OPEN ACCESS
OPUS AUGSBURG

Universität Augsburg
Universitätsbibliothek

Evolutionary trajectories of IDHWT glioblastomas reveal a common path of early tumorigenesis instigated years ahead of initial diagnosis

Verena Körber, Jing Yang, Pankaj Barah, Yonghe Wu, Damian Stichel, Zuguang Gu, Michael Nai Chung Fletcher, David Jones, Bettina Hentschel, Katrin Lamszus, Jörg Christian Tonn, Gabriele Schackert, Michael Sabel, Jörg Felsberg, Angela Zacher, Kerstin Kaulich, Daniel Hübschmann, Christel Herold-Mende, Andreas von Deimling, Michael Weller, Bernhard Radlwimmer, Matthias Schlesner, Guido Reifenberger, Thomas Höfer, Peter Lichter

Angaben zur Veröffentlichung / Publication details:

Körber, Verena, Jing Yang, Pankaj Barah, Yonghe Wu, Damian Stichel, Zuguang Gu, Michael Nai Chung Fletcher, et al. 2019. "Evolutionary trajectories of IDHWT glioblastomas reveal a common path of early tumorigenesis instigated years ahead of initial diagnosis." Cancer Cell 35 (4): 692–704.e12. https://doi.org/10.1016/j.ccell.2019.02.007.

Nutzungsbedingungen / Terms of use: **CC BY-NC-ND 4.0**

Dieses Dokument wird unter folgenden Bedingungen zur Verfügung gestellt: / This document is made available under these conditions:
CC-BY-NC-ND 4.0: Creative Commons: Namensnennung - Nicht kommerziell - Keine Bearbeitung
Weitere Informationen finden Sie unter: / For more information see:
https://creativecommons.org/licenses/by-nc-nd/4.0/deed.de

Evolutionary Trajectories of IDH^{WT} Glioblastomas Reveal a Common Path of Early Tumorigenesis Instigated Years ahead of Initial Diagnosis

Verena Körber,[1,2] Jing Yang,[3,4] Pankaj Barah,[3] Yonghe Wu,[5,7] Damian Stichel,[6] Zuguang Gu,[3,7] Michael Nai Chung Fletcher,[5] David Jones,[8] Bettina Hentschel,[9] Katrin Lamszus,[10] Jörg Christian Tonn,[11] Gabriele Schackert,[12] Michael Sabel,[13] Jörg Felsberg,[14] Angela Zacher,[14] Kerstin Kaulich,[14] Daniel Hübschmann,[3] Christel Herold-Mende,[15] Andreas von Deimling,[6] Michael Weller,[16] Bernhard Radlwimmer,[5] Matthias Schlesner,[4] Guido Reifenberger,[14,*] Thomas Höfer,[1,2,*] and Peter Lichter[5,7,17,*]

[1]Division of Theoretical Systems Biology, German Cancer Research Center (DKFZ), Im Neuenheimer Feld 280, 69120 Heidelberg, Germany
[2]Bioquant Center, Heidelberg University, Im Neuenheimer Feld 267, 69120 Heidelberg, Germany
[3]Division of Theoretical Bioinformatics, German Cancer Research Center (DKFZ), Im Neuenheimer Feld 280, 69120 Heidelberg, Germany
[4]Bioinformatics and Omics Data Analytics, German Cancer Research Center (DKFZ), Im Neuenheimer Feld 280, 69120 Heidelberg, Germany
[5]Division of Molecular Genetics, German Cancer Research Consortium (DKTK), German Cancer Research Center (DKFZ), Im Neuenheimer Feld 280, 69120 Heidelberg, Germany
[6]Clinical Cooperation Unit Neuropathology, German Cancer Research Center (DKFZ), Im Neuenheimer Feld 280, 69120 Heidelberg, Germany
[7]Heidelberg Center for Personalized Oncology, DKFZ-HIPO, German Cancer Research Center (DKFZ), Im Neuenheimer Feld 280, 69120 Heidelberg, Germany
[8]Pediatric Glioma Research, German Cancer Research Center (DKFZ), Im Neuenheimer Feld 280, 69120 Heidelberg, Germany
[9]Institut für Medizinische Informatik, Statistik und Epidemiologie, Universität Leipzig, Härtelstr. 16-18, 04107 Leipzig, Germany
[10]Department of Neurosurgery, University Medical Center Hamburg-Eppendorf, Neues Klinikum O10, Martinistr. 52, 20246 Hamburg, Germany
[11]Department of Neurosurgery, Ludwig Maximilians University Munich and German Cancer Consortium (DKTK), partner site Munich, Marchioninistraße 15, 81377 Munich, Germany
[12]Department of Neurosurgery, Technical University Dresden, Fetscherstr. 74, 01307 Dresden, Germany
[13]Department of Neurosurgery, Heinrich Heine University Düsseldorf, Moorenstr. 5, 40255 Düsseldorf, Germany
[14]Institute of Neuropathology, Heinrich Heine University Düsseldorf, and German Cancer Consortium (DKTK), partner site Essen/Düsseldorf, Moorenstr. 5, 40255 Düsseldorf, Germany
[15]Department of Neurosurgery, Heidelberg University Hospital, Im Neuenheimer Feld 400, 69120 Heidelberg, Germany
[16]Department of Neurology, University Hospital Zurich, Frauenklinikstr. 26, 8091 Zurich, Switzerland
[17]Lead Contact
*Correspondence: guido.reifenberger@med.uni-duesseldorf.de (G.R.), t.hoefer@dkfz.de (T.H.), peter.lichter@dkfz.de (P.L.)

SUMMARY

We studied how intratumoral genetic heterogeneity shapes tumor growth and therapy response for isocitrate dehydrogenase (IDH)-wild-type glioblastoma, a rapidly regrowing tumor. We inferred the evolutionary trajectories of matched pairs of primary and relapsed tumors based on deep whole-genome-sequencing data. This analysis suggests both a distant origin of *de novo* glioblastoma, up to 7 years before diagnosis, and a common path of early tumorigenesis, with one or more of chromosome 7 gain, 9p loss, or 10 loss, at tumor initiation. *TERT* promoter mutations often occurred later as a prerequisite for rapid growth. In contrast to this common early path, relapsed tumors acquired no stereotypical pattern of mutations and typically regrew from oligoclonal origins, suggesting sparse selective pressure by therapeutic measures.

INTRODUCTION

Tumors are typically heterogeneous mixtures of genetic subclones. Analyses of subclonal tumor evolution have focused on oncogenic drivers, which may inform the search for more effective therapeutic approaches (Greaves and Maley, 2012). However, recent studies have questioned this idea by arguing that much of the intratumoral genetic heterogeneity is due to neutral mutations (Williams et al., 2016; Ling et al., 2015). As tumor growth as a whole is caused by driver mutations, these findings concern the fundamental, but poorly understood, question of the relation between tumor growth and genetic evolution.

Glioblastoma is the most frequent malignant primary brain cancer in adults that rapidly recurs after initial therapy (with a 5-year survival of 6%; Ostrom et al., 2016). Thus, it is of particular clinical interest whether standard chemoradiotherapy exerts selective pressure on the evolution of the relapse tumor. Several studies have suggested that branched clonal evolution of glioblastomas contributes to treatment failure (Francis et al., 2014; Hu et al., 2017; Meyer et al., 2013; Patel et al., 2014; Snuderl et al., 2011; Sottoriva et al., 2013; Wang et al., 2016). In this view, surgical tumor resection followed by chemoradiotherapy with temozolomide (TMZ) (Weller et al., 2017) may select resistant subclones from residual tumor cells that quickly regrow (Gerlinger and Swanton, 2010; Nathanson et al., 2014; Qazi et al., 2017). Moreover, Johnson et al. (2014) showed that TMZ treatment may drive the evolution of isocitrate dehydrogenase (IDH)-mutant diffuse gliomas to more malignant stages. Here we investigate genetic evolution of IDH-wild-type (IDH^{WT}) glioblastomas and its relation to tumor relapse following initial therapy.

RESULTS

Mutation Patterns in Primary and Recurrent Glioblastomas Are Largely Similar

To assess the genetic evolution of glioblastomas, we analyzed the genomes, transcriptomes, and methylomes in paired primary (untreated) and recurrent (following initial treatment) tumor tissue samples from patients with *de novo* glioblastomas, IDH^{WT}, World Health Organization grade IV. In total, paired tissue samples from 50 patients were included, most of whom had received radiotherapy combined with concomitant and maintenance TMZ chemotherapy after neurosurgical resection (Figure 1A; Table S1). We sequenced whole genomes of 21 tumor pairs (149× average coverage; discovery set) and a matched blood control (78× average coverage), as well as the transcriptomes of primary and recurrent tumors (Figure 1B). The median tumor cell contents were 80% and 78% for primary and recurrent samples, respectively (Figure S1A). Transcriptome and methylome analyses indicated that the vast majority of non-tumor cells were infiltrating immune cells, particularly monocytes (Figures S1B and S1C) (Wang et al., 2017). In addition, we sequenced a panel of 50 glioma-associated genes in primary and recurrent tumor pairs from 43 IDH^{WT} glioblastoma patients (Table S1; validation set). Assessing genome-wide DNA methylation patterns in both sets with Illumina 450k/EPIC bead chip arrays, we found the previously described major glioblastoma subgroups by unsupervised clustering (Figure 1B; Capper et al., 2018; Sturm et al., 2012). Samples classified as mesenchymal subtype had comparatively low tumor content, suggesting that this particular classification may be influenced by a higher fraction of non-tumor cells. When excluding subtype switches involving the mesenchymal subtype, we found that 90% of primary and recurrent tumor pairs had a stable methylation subtype, while the remainder switched from the RTKII to the RTKI group (Figures 1B and S1D).

Whole-genome sequencing yielded a median mutational burden of 12,800 somatic single nucleotide variants (SNVs) and small insertions/deletions (indels) per tumor (Figure 1C). One primary and four recurrent tumors had vastly more mutations ($>10^5$), which included somatic mutations in DNA mismatch repair genes (*MLH1* or *MSH6*) that are consistent with a hypermutation genotype. Apart from these hypermutated cases, primary and recurrent tumor samples had comparable numbers of mutations ($p = 0.77$, two-sided Welch two-sample t-test). On average, about as many mutations were shared between primary and recurrent samples as were private to either sample (Figures 1D and 1E). The shared mutations were dominated by the clock-like mutational signature 1 (Figure 1F; Alexandrov et al., 2013; Forbes et al., 2016). The pattern of private mutational signatures in both primary and non-hypermutated recurrent tumors were shifted away from signature 1 and included signatures due to defective double-strand break repair by homologous recombination (signature 3), defective mismatch repair (signature 15 and signature 26) and one of unknown etiology (signature 5) (Figure 1G). The hypermutated tumors were dominated by mutational signature 11 (Figure 1H) linked to TMZ treatment (Alexandrov et al., 2013). The similarity of mutation counts and signatures in paired primary and recurrent tumors suggests that the major part of the genetic evolution occurred prior to the diagnosis of the primary tumor. Only the comparatively small subgroup of hypermutated tumors showed a global mutational signature of cytotoxic treatment.

Paucity of Common Mutations in Recurrent Tumors

We identified recurrent driver mutations in SNVs, indels, copy number variations (CNVs) and structural variants, several of which are druggable (Figure S2A) (Gröbner et al., 2018). Driver mutations detectable in tumors of at least three patients were found in the coding regions of 28 genes, in 13 non-coding RNA genes, and in the *TERT* promoter region (Figure 2A). All 21 tumor pairs harbored at least one of three chromosomal gains or losses: (1) loss of the entire or the q arm of chromosome 10, including the *PTEN* locus; (2) loss of the p arm of chromosome 9 or focal deletion of the *CDKN2A/B* locus; (3) complete or partial gain of chromosome 7, including the *EGFR* locus (Figures 2A and 2B). Most of 9p losses and focal deletions of *CDKN2A/B* were homozygous. Chromosome 10 or 10q losses were always hemizygous but in 75% of the tumor samples accompanied by a mutation in the remaining *PTEN* allele. Chromosome 7 gains were frequently (58%) accompanied by focal amplifications of the *EGFR* locus (which may be extrachromosomal in the form of double minutes; deCarvalho et al., 2018). When present, focal *EGFR* amplification occurred

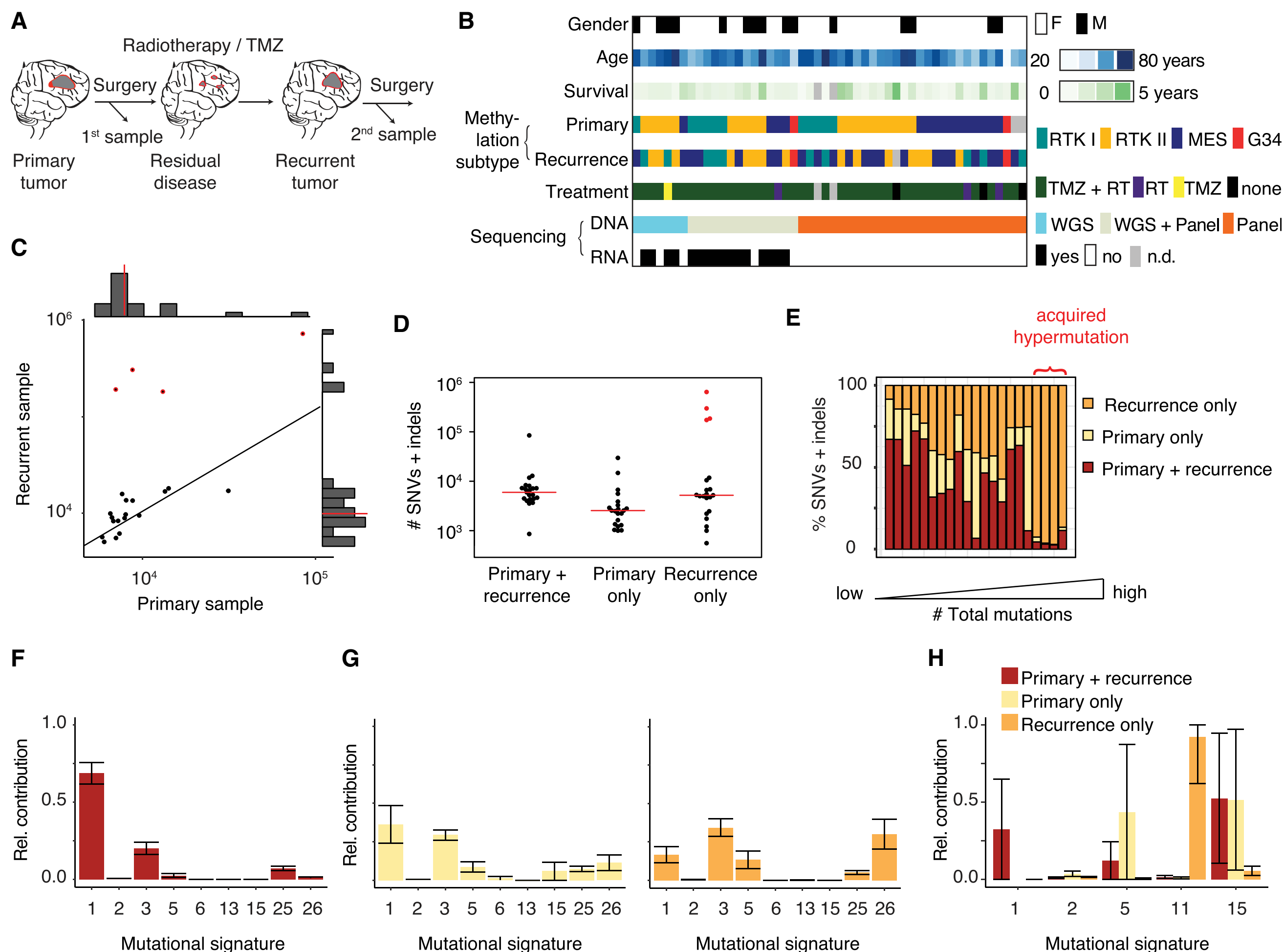

Figure 1. Clinical Data and Mutation Statistics

(A) Sampling strategy.

(B) Overview of clinical parameters and sequencing approaches.

(C) Number of SNVs and small insertions/deletions called in primary and recurrent samples of the discovery set (red lines, median; red dots, hypermutated cases).

(D) Numbers of common and private SNVs and small insertions/deletions of the discovery set (red lines, median; red dots, hypermutated cases).

(E) Relative numbers corresponding to (D) per tumor.

(F–H) Mutational signatures of shared (F) and private SNVs, (G) (left, primary; right, relapsed) from non-hypermutated cases of the discovery set as well as mutational signatures of hypermutated cases (H). Data are represented as means ± SEM.

See also Figure S1 and Table S1.

in all but one case already in the primary tumor and was lost in 27% of recurrent samples. Almost half of the *EGFR* amplifications (44%) co-occurred with the active variant EGFRvIII (generated by deletion of exons 2–7; Brennan et al., 2013), and in three samples *EGFR* had an interchromosomal translocation into the vicinity of a superenhancer (Figure 2C). In several cases chromosomal gains increased (Figure 2D) or decreased (Figure 2E) in complexity between primary and recurrent tumors.

TERT promoter mutations were found in all but one primary sample. In contrast to chromosomal gains/losses and the *TERT* promoter mutations, the most frequent coding mutations (occurring in *PTEN*, *EGFR*, or *TP53*) were present in a subset of the tumors only. We observed comparable distributions of SNVs and small indels in these genes, as well as *TERT* promoter mutations, in the validation set (Figure S2B). Moreover, mutations in 13 non-coding RNA genes were recurrent, including *HOTTIP*, *SNHG14*, *KCNQ1OT1*, and *XIST* previously implicated in cancer (Cheng et al., 2017; Jin et al., 2017; Wang et al., 2018; Yao et al., 2015). The occurrence of widespread driver mutations in primary tumors that are maintained in the corresponding recurrent tumors (*PTEN*, *CDKN2A/B*, and *EGFR* mutations as well as mutations in the *TERT* promoter) contrasted with a paucity of common mutations newly detected in the recurrent tumor samples. Except for mutations in the mismatch repair gene *MSH6* and in *XIST*, which were enriched in the hypermutated recurrent samples, no recurrent mutations were preferentially found upon glioblastoma recurrence (note that hypermutated tumors have a higher probability for recurrence of mutations by chance). There were, however, several cases of

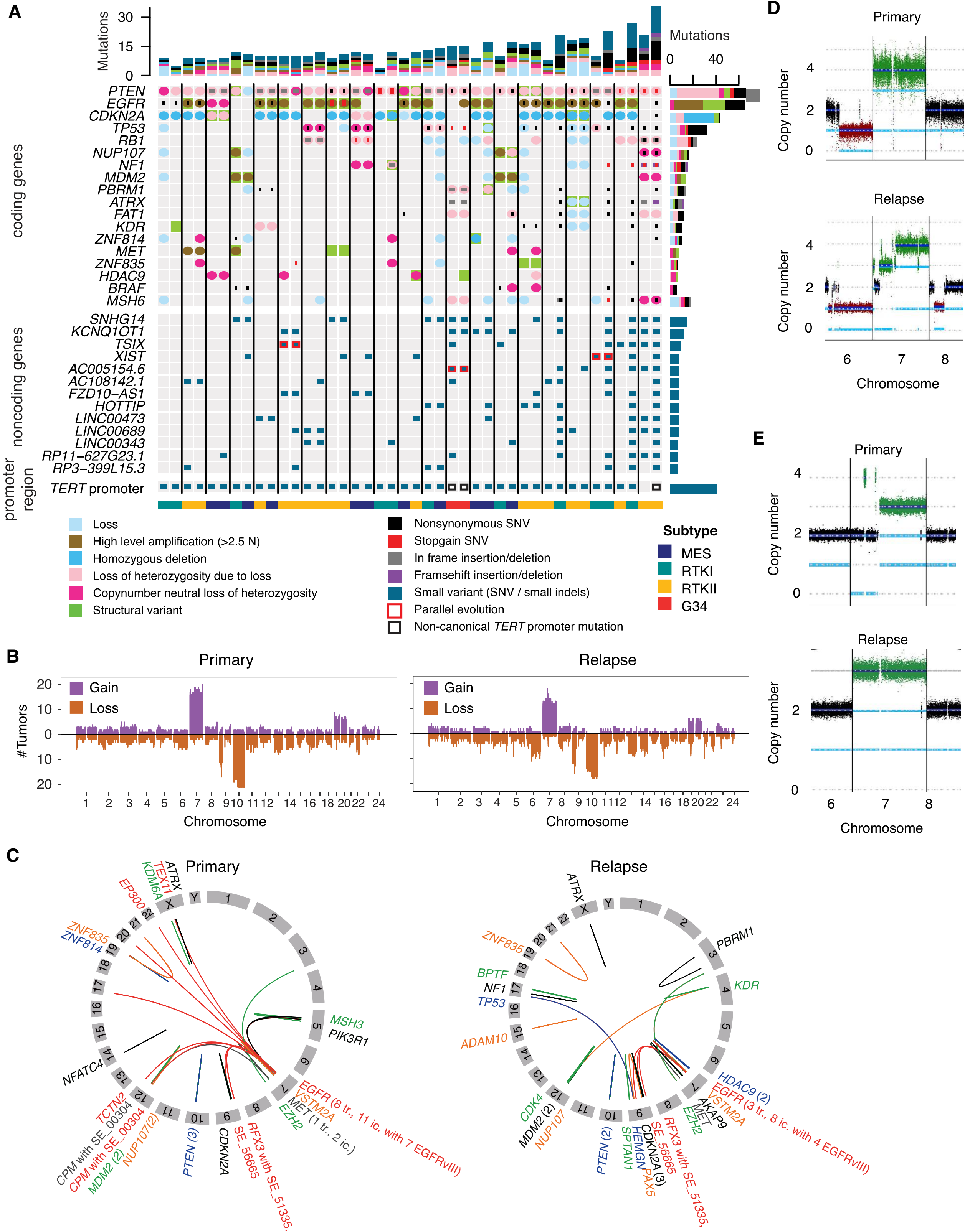

(legend on next page)

parallel evolution. We found different mutations in pairs of primary and recurrent samples for the following eight driver genes: *EGFR* (5 pairs), *ARID1A*, *AC005154.6*, *KCNQ1OT1*, *PTEN, PTPN11*, *TSIX*, and *XIST* (one pair each).

Genetic Evolution of Glioblastoma Shows a Common Pattern across DNA Methylation Subtypes

To understand how the mutation patterns in primary and recurrent glioblastomas arose, we inferred evolutionary histories for the individual sample pairs. We determined for each sample the allele frequencies of SNVs and indels (variant allele frequencies [VAFs]) at non-amplified loci. Mutations present in both primary and recurrent tumors showed a wide range of VAFs (Figure 3A). Many shared mutations will have arisen comparatively early in tumor development and will therefore be clonal in both samples. Based on the read coverage of a given locus, we tested with a binomial model whether a measured VAF is compatible with sampling from a VAF of 50%, implying that the respective allele is clonal. While this test minimizes erroneous assignment of a mutation as subclonal, we found subclonality in both primary and recurrent samples for 12% of shared mutations (Figure 3A, red dots). An additional 7% of mutations were identified as clonal in the primary tumor and subclonal in the recurrent tumor (Figure 3A, orange dots). This outcome is not possible for a tumor with a single origin and hence was most likely due to undersampling of the primary tumor, effectively augmenting the count of subclonal mutations. Finally, a transition from subclonality in primary to clonality in the recurrent tumors is suggested for 11% of shared mutations (Figure 3A, blue dots), which may result from undersampling of the recurrent tumor (STAR Methods, Subclonality test), surgical resection retaining a particular subclone that then forms a clonal recurrence (see Figure 3H below), or genetic evolution. Taken together, the VAF analysis indicates extensive subclonality of shared mutations in pairs of primary and recurrent glioblastoma tissue samples.

Subclonality is informative on tumor evolution. To uncover this information, we mapped the observed intratumoral genetic heterogeneity onto the subclonal phylogeny of primary and recurrent tumors. We combined SNVs and CNVs, developing a likelihood-based multinomial model that jointly infers genetically distinct subpopulations and their phylogenetic relationships from the sequencing read count distribution over all mutated loci (Figures 3B, S3A, and S3B). We assessed the robustness of our algorithm on simulated data with characteristics of the measured data and found reliable detection of even small clones (5% clone size detected with >80% sensitivity) and faithful inference of subclonal phylogenies (Figures S3C–S3K). We then applied subclonal inference to the measured data, treating normal tissue as an additional subclone, and found that the estimated tumor cell content closely agreed with purity estimates from ACEseq (Pearson's r = 0.95, Figure S3L). Thus our likelihood-based inference method performed well with simulated data and reproduced the independent estimate of tumor cell content in the actual data.

We determined the subclonal structure jointly for pairs of primary and recurrent tumor samples and typically resolved two to three subclones per sample (Figure 3C), with a clear hierarchy of clone sizes (Figure 3D). Allowing for up to five subclones per tumor sample did not alter the best-fit tree in all but two cases; in the latter two cases additional subclones were added within the already existing tree structure. Thus the resolution of up to three subclones per sample allowed reliable placement of driver mutations in tumor phylogenies.

In 15 out of 21 of the sample pairs the recurrent tumor originated from more than one clone of the primary tumor (oligoclonal origin of the relapse; Figures 3E–3G, S4A, and S4B). Figure 3E introduces the layout of the phylogenetic trees. Note that, due to limited sampling, the evolution of a recurrent tumor subclone in the inferred phylogenetic trees does not start directly with the corresponding subclone in the primary tumor but, instead, both subclones have an unobserved common ancestor. Figure 3F shows a typical example, where one allele of *PTEN* was lost (chromosome 10 loss) and the other one was inactivated by a mutation, before subclonal branching became evident. Subclonal evolution in the primary tumor added further potential drivers, notably a partial gain of chromosome 7 (including *EGFR*) and mutations in the *TERT* promoter, *BRAF* (D594G) and *TSIX*. The recurrent tumor arose from two subclones of the primary tumor and showed further, subclone-specific driver mutations. Figure 3G depicts an extreme case of oligoclonal relapse where no further recurrent drivers developed within 307 days between primary and recurrent resection of the tumor (median time span between initial diagnosis and relapse 284 days). In 6 of 21 cases the relapse tumor had a monoclonal origin (Figures 3H and S4C). However, this might be partially due to taking experimental samples and, indeed, we found only one clear example of linear evolution of the recurrent tumor, with several new driver mutations being acquired over a comparatively large time span of $\sim$22 months between primary and secondary

Figure 2. Recurrent Driver Mutations In Paired Primary and Recurrent Tumor Samples from 21 Glioblastoma Patients

(A) Mutational spectrum in likely driver genes. Coding genes are shown if targeted by a structural variation, SNV, indel, homozygous deletion, or a high-level amplification in at least two patients (excluding hypermutated samples; mutations in *MSH6* are additionally shown due to their correlation with a hypermutation genotype). Non-coding genes are shown if targeted by an SNV or an insertion/deletion in more than five patients. *TERT* promoter mutations are shown at the bottom. Primary and recurrent samples of a tumor are shown in pairs and separated by vertical lines (left, primary; right, recurrent). Different colors mark different types of mutations while the color code at the bottom indicates DNA methylation subtypes.

(B) Chromosomal gains and losses in primary and relapsed tumors.

(C) Inter-chromosomal and intra-chromosomal structural variants in primary and relapsed tumors. Translocation partners are marked if targeting a gene or the vicinity of a super-enhancer (based on dbSUPER; Khan and Zhang, 2016). Genes targeted by intra-chromosomal variants are highlighted if they were present in the driver genes list. Numbers in brackets indicate the number of recurrences of a structural variant (tr., inter-chromosomal translocation; ic., intra-chromosomal variant).

(D and E) Two examples of ongoing evolution on chromosome 7. Both cases can be explained by an initial gain of the chromosome, followed by partial losses in the recurrent (D) or the primary tumor (E) (black, normal copy number; green, gains; red, losses; light blue lines, number of A- and B-alleles).

See also Figure S2.

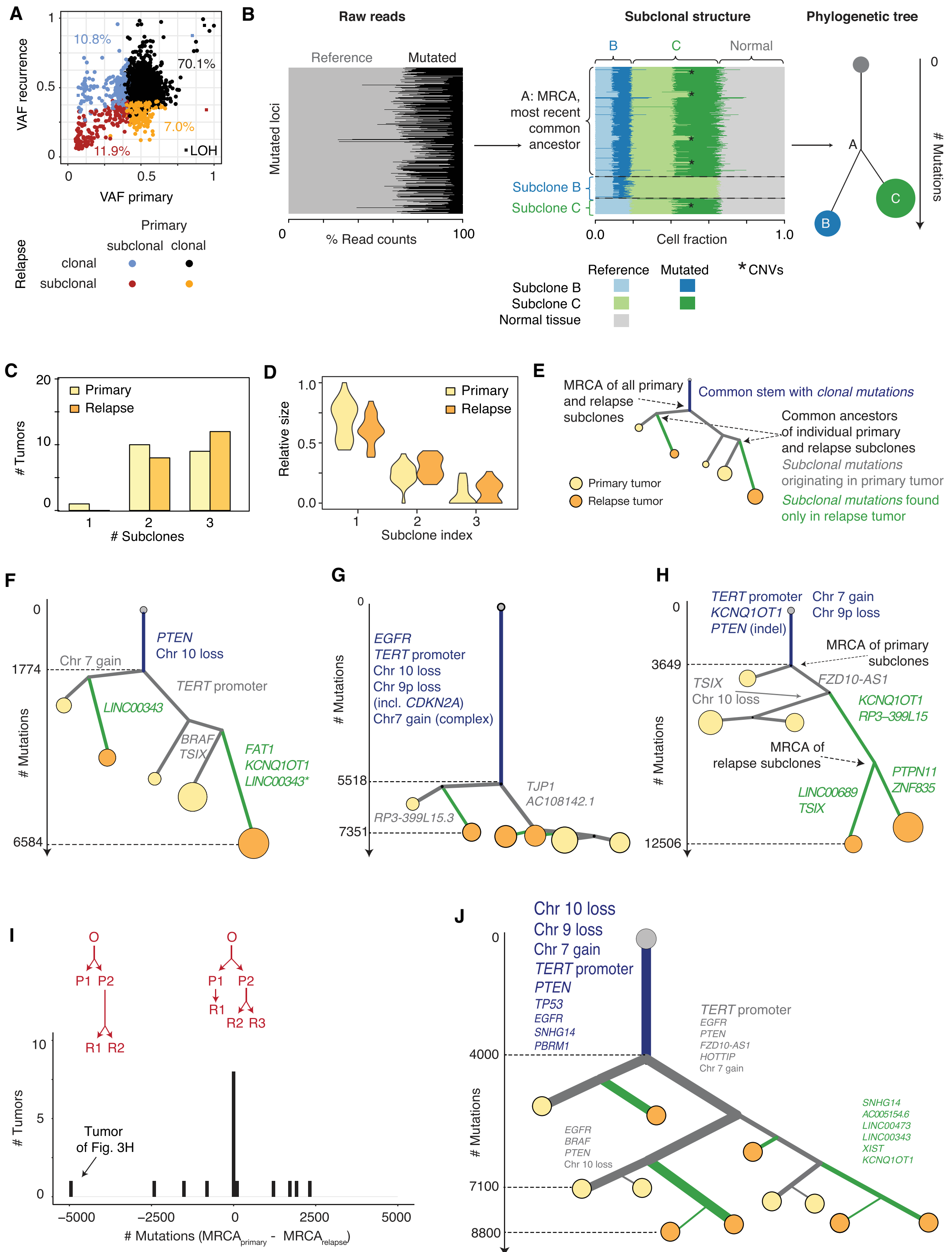

Figure 3. Phylogenetic Inference

(A) Variant allele frequencies at loci with normal copy numbers (excluding hypermutated samples and, for clarity, showing mutations in functional regions only). Clonal and subclonal mutations were classified based on a binomial test for clonality (significance level $\alpha = 0.05$).

(legend continued on next page)

resection (Figure 3H). In this case, the evolutionary time (measured by the number of mutations between the most recent common ancestors of the subclones in the primary and recurrent tumors) was indeed comparatively large (~5,000 mutations). In contrast to this unique case, the other tumor pairs had identical, or very similar, evolutionary times of emergence of primary and relapse subclones (Figure 3I). Hence recurrent tumors mainly emerged from already established heterogeneity of the primary tumor and only moderately added to that. This common pattern of glioblastoma evolution was independent of DNA methylation subtype and, in particular, also methylation status of the *MGMT* promoter associated with response to TMZ therapy (Hegi et al., 2005). To derive a consensus phylogeny over all analyzed tumors, we walked down the phylogenetic trees from the common stem and scaled branch thickness according to the number of branch occurrences over all trees, revealing a typical pattern of each primary subclone spawning a corresponding relapse subclone (Figure 3J). The frequency of recurrent mutations declined rapidly from the common stem toward the branches, suggesting that therapeutic measures do not drive preferential resistance scenarios.

CNVs Precede SNVs as Oncogenic Drivers

Clonal mutations map to the common stem of the phylogenetic tree and, for each tumor, contain recurrent driver mutations, which likely are of early origin in the evolution of the tumor. Further driver mutations were subclonal and hence originated more recently than the drivers in the stem. Most subclones in relapsed tumors (77%) showed additional driver mutations that were not found in the primary tumor samples, indicating ongoing genetic evolution.

We found strong overrepresentation of gain of chromosome 7, loss of chromosome arm 9p/focal loss of *CDKN2A/B*, and loss of chromosome 10/10q in the common stem of the phylogenetic trees, with at least one of these chromosomal gains or losses being clonal in 20 out of 21 tumor pairs (Figure 4A). The single tumor, where none of these chromosomal aberrations was clonal, harbored two recurrent mutations (as in Figure 2) at the clonal level, a frameshift insertion in *PTEN* and a clonal SNV in exon 7 of *TP53* (Pro > Ser; 278 amino acids). The most prominent oncogenes on the altered chromosomes are *EGFR* (chromosome 7), *CDKN2A/B* (chromosome 9), and *PTEN* (chromosome 10), suggesting that mutations and/or CNVs in these three genes define the minimal set of driver mutations from which at least one, and frequently two or all (81%), occur in the stem of each analyzed tumor. Hence these mutations might be early tumorigenic events.

In contrast to the CNVs, most recurrent SNVs were subclonal, with the exceptions of mutations in *TP53, PTEN, EGFR*, and the *TERT* promoter (Figure 4B). Notably, most clonal *PTEN* mutations (7/10) co-occurred with a loss of the other *PTEN* allele. Mutations in the *TERT* promoter occurred in all but one of the 42 primary and recurrent samples, but, remarkably, were subclonal in 33% of them. Of note, the read coverage of the GC-rich *TERT* promoter was uniformly high (123× on average), allowing accurate VAF estimation; moreover, comparison of the VAF distribution of the *TERT* promoter mutations with a control set of heterozygous germline mutations, including a germline SNP in the *TERT* promoter region, clearly showed significant subclonality in the former (Figures S5A–S5E). Nevertheless, in all but one case subclonal *TERT* promoter mutations occurred in the primary tumor. In addition to canonical *TERT* promoter mutations reported previously, we also found exclusively "non-canonical" promoter mutations in two tumors (Figure 4C). These tumors also had clonal mutations in *ATRX*, which inhibits alternative telomere lengthening (exonic frameshift generating a premature stop codon). Analyzing one such case in detail, we found that the *ATRX* mutation likely supported tumor growth, as the protein was lost (Figure S5F), whereas the non-canonical *TERT* promoter mutation did not increase transcript levels compared with non-tumor brain tissue (Figure S5G). These and further data (Figure S5H) are consistent with the view that *ATRX* mutations and canonical *TERT* promoter mutations are independent mechanisms to support survival of proliferating tumor cells.

Taken together, the placement of mutations on the phylogenetic trees indicates characteristic patterns of their occurrence: CNVs in chromosomes 7, 9, or 10 generally took place early in the evolution of the tumor while *TERT* promoter mutations were often acquired subsequently in primary tumors, remaining subclonal in one-third of them. The absence of mutations that

(B) Principle of phylogenetic inference from whole-genome sequencing data, with fractions of mutated and reference reads at mutated loci, the inferred subclonal distribution and the resulting phylogenetic tree. The mutated DNA fraction within tumor subclones is indicated by a darker shading; stars mark examples of loci with copy number changes. The data shown are for the two subclones of the recurrent tumor in (H).

(C and D) Summary statistics on inferred phylogenies, with number of subclones (C) and their relative sizes (D), the width of the violin plots indicate the frequency of a given clone size.

(E) Layout of phylogenetic trees. Vertical branch lengths scale with the number of mutations, circle areas scale with relative subclone sizes.

(F and G) Examples of phylogenetic trees with oligoclonal origin of the recurrent tumor, with (F) and without (G) recurrent driver mutations acquired after primary resection (yellow, primary tumor; orange, recurrent tumor; blue branches, common stem; gray branches, mutations originating in primary tumor; green branches, mutations found only in relapse tumor; asterisk marks convergent evolution; mutations in driver genes and copy number changes of chromosomes 7, 9, and 10 are indicated).

(H) Monoclonal origin of the recurrent tumor; primary and recurrent tumors are separated by a long branch and several new driver mutations (mutations in driver genes and copy number changes of chromosomes 7, 9, and 10 are indicated).

(I) Origin of the recurrent tumor relative to origin of the primary tumor (excluding hypermutated cases). The distance between the most recent common ancestors (MRCA) of primary and recurrent samples (measured in mutation counts) is provided as a measure for tumor origin.

(J) Consensus tree of all sample pairs. Branch widths and font sizes scale with the number of cases supporting a connection and mutation, respectively. The median number of clonal mutations and the median of the maximal number of mutations per subclone are indicated for primary and recurrent tumors. Driver mutations are indicated at particular tree branches (distinguishing clonal, subclonal, present in primary or recurrence only) if they are found there in at least two tumors and are frequent overall (present at any position in at least three [coding genes] or five [non-coding genes] non-hypermutated tumors).

All data are from the discovery set subjected to deep whole-genome sequencing (WGS).

See also Figures S3 and S4.

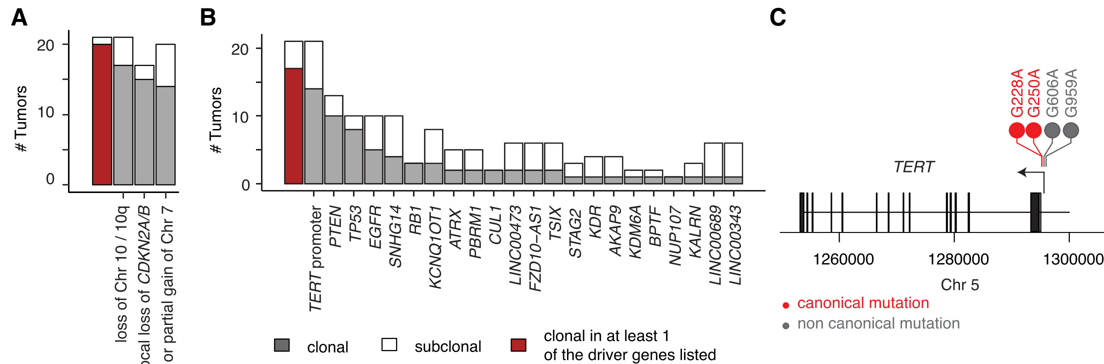

Figure 4. Patterns of Mutations during Different Stages of Tumorigenesis

(A) Number of clonal and subclonal copy number changes on chromosomes 7, 9, and 10.

(B) Number of clonal and subclonal mutations (SNVs and indels) in driver genes that were clonal in at least one tumor. Red bars represent the numbers of tumors harboring at least one of the listed driver mutations clonally. In a few cases, mutations could not unambiguously be placed on the phylogenetic trees as clonal or subclonal; these were counted as clonal when the probability of placing them in the tumor stem was >10%.

(C) Canonical (red) and non-canonical (gray) mutations in the *TERT* promoter region.

All data are from the discovery set subjected to deep WGS.

See also Figure S5.

are characteristic for recurrent tumors may indicate that little directed selective pressure is exerted by chemotherapy and/or radiotherapy.

Large Selective Advantage of *TERT* Promoter Mutations

We reasoned that combining data on the number of somatic mutations accumulated during tumor evolution with estimates of the characteristic tumor size upon primary resection and the somatic mutation rate will yield insight into the evolution of IDH^{WT} glioblastoma. Tumor growth results from the balance of cell proliferation and death rates, whereas the bulk of mutations is assumed to occur during cell proliferation (Figure 5A). A human brain tumor of 20 cm^3 or larger (Goldberg-Zimring et al., 2005) corresponds to at least 10^9–10^{10} cells (Del Monte, 2009; DeVita et al., 1975; Milo et al., 2010). The number of somatic mutations in a primary tumor cell (M) is the sum of mutations that were already present when the first oncogenic event occurred in the founder cell (M_1) and the mutations that occurred subsequently during tumor evolution (M_2). Hence, to obtain the mutation number of interest, M_2, we subtract M_1 from M. We get conservative estimates of M and M_1 from the whole-genome sequencing (WGS) data as follows: M_1 is taken as the number of mutations in the tumor stem (clonal mutations, M_C) while M is taken as the average number of mutations in all subclones of the primary tumor; hence, the clonal and subclonal mutation counts provide a measure of evolutionary time (Figure 5B). Excluding hypermutated cases, we find a median of M_2 = 2,300 mutations accumulated during the evolution of the primary tumor (Figure S5I). Subclonal mutations became fixed through cell divisions, and we assume a constant rate of mutation accumulation per division. The average somatic mutation rate was taken as 2.6×10^{-9} per base pair and division (Milholland et al., 2017), which corresponds primarily to the clock-like mutation signature in our data (Figure 1F; signature 1). We observed a drop of the signature 1 contribution by 77% between clonal mutations (tumor stem) and late mutations (at the tips of the phylogenetic trees; Figure S5J), which implies an increase in mutation rate during tumor evolution provided that the clock-like rate is constant. Therefore, we accounted for the possibility of a 4-fold increase of the somatic mutation rate during tumor evolution. To accumulate 2,300 mutations with this range of mutation rates (2.6×10^{-9} to 10.6×10^{-9} mutations per base pair and division), 66–268 cell divisions are required. To then reach a realistic tumor size of 10^9–10^{10} cells, most daughter cells (69%–92%) must have died eventually (Figures 5C, S5K, and S5L). Hence, the combined balance of cell numbers and somatic mutations implies that massive cell death occurs during glioblastoma evolution and, on average, only 8%–31% of cell divisions lead to tumor growth (Figures S5K and S5L).

The estimated high fraction of cell death is an average over the entire time course of evolution up to the resected primary tumor. Our WGS data show that a core set of pro-proliferative driver mutations (CNVs affecting *CDKN2A/B*, *PTEN*, or *EGFR*) occurred early during tumor evolution. *TERT* promoter mutations were also found in all but one primary tumor, but their frequent subclonality indicates that they may occur subsequent to tumor initiation. These mutations have been described as a key event that extends cellular lifespan by healing short telomeres (Chiba et al., 2017). We modeled this scenario by assuming an initial growth regime with massive cell death before the *TERT* promoter mutation and, thereafter, a second regime with reduced cell death (Figure 5D). This model reproduced the observed distribution of tumors with clonal and subclonal canonical *TERT* promoter mutations (chr5:1295228/chr5:1295250) provided that these mutations reduced the cell death rate by 6%–26% (Figures 5E, S5M, and S5N), corresponding to a

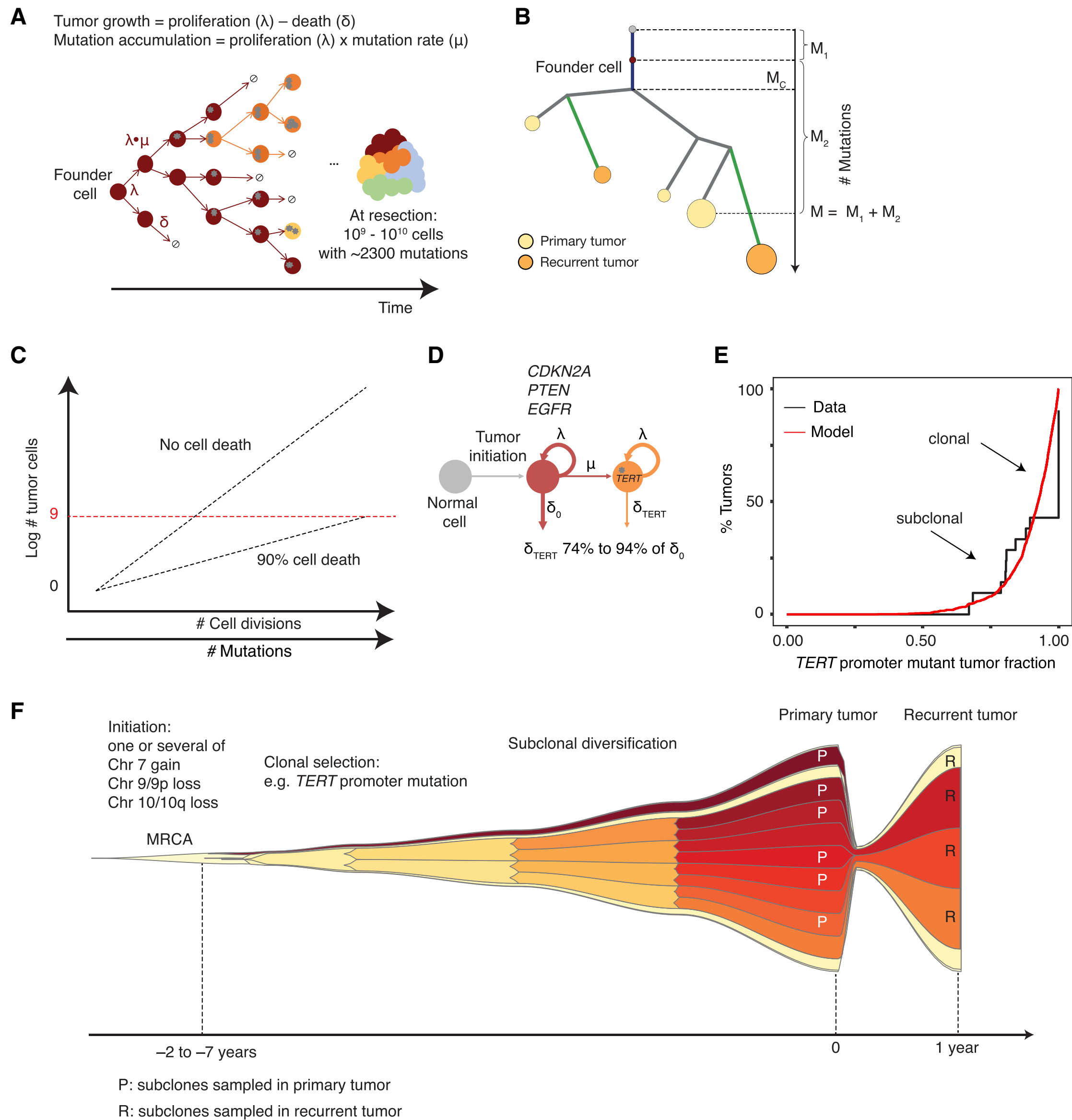

Figure 5. Evolutionary Dynamics during Glioblastoma Growth

(A) Model of tumor growth. Cells divide at rate λ, die at rate δ, and accumulate mutations at rate $\lambda\mu$. Clinically detectable tumors have cell counts in the order of 10^9 to 10^{10}, each of which on average accumulated 2,300 mutations between tumor initiation and clinical detection (median of 17 non-hypermutated tumors).

(B) Schematic of the mutation counts used for rate estimation. Tumors are initiated by a somatic cell with M_1 prior (neutral) mutations. Extant subclonal diversification occurs after M_C mutations (i.e., at the most recent common ancestor of the tumor). Individual cells accumulate additional mutations during tumor growth (resulting in a total of M mutations per cell at clinical presentation).

(C) The numbers of cell divisions and mutations scale logarithmically with the number of tumor cells. The slope of the growth curve is determined by the rate of cell death. Hence knowledge of tumor cell number and number of cell divisions allows to infer the rate of cell death.

(D) Model for the acquisition of canonical *TERT* promoter mutations during glioblastoma evolution. A transformed cell divides due to initial pro-proliferative mutations (including the common CNVs in the tumor stem). After capturing an additional *TERT* promoter mutation with probability μ dt, the cellular death rate is reduced to δ_{TERT}.

(E) Inferred and modeled cumulative distribution of the tumor fraction with canonical *TERT* promoter mutation (estimated from its most likely position in the phylogenetic trees of the 19 cases with canonical *TERT* promoter mutation).

(F) Model of glioblastoma growth (individual subclones are labeled by different shades of yellow to red for clearer distinction; MRCA, most recent common ancestor).

See also Figure S5.

selective advantage of 0.03–0.16. While this is an upper estimate because further mutations may have contributed to reducing cell death, the frequency of *TERT* promoter mutations is not matched by any other subclonal mutation, thus suggesting that other mutations are unlikely to have been major contributors. Notably, the selective advantage of *TERT* promoter mutations

is larger than the average number for driver mutations (0.004; Bozic et al., 2016).

Finally, we estimated the time duration between the emergence of the founder cell and tumor diagnosis. To this end, we determined the average division rate of the tumor cells by dividing the number of mutations occurring after primary resection by the mutation rate and the time between primary and secondary resection. This yielded a lower bound of tumor cell division rate of approximately once in 10 days. With the number of cell divisions given above that establish the primary tumor, we find that the founder cell emerges approximately 2–7 years prior to diagnosis (Figure 5F). This range indicates that IDH^{WT} glioblastomas may undergo several years of evolution before being detected.

DISCUSSION

The fast and incurable tumor recurrence in IDH^{WT} glioblastomas underlines the need for more effective treatment approaches. Reconstructing the evolutionary histories of matched pairs of primary and recurrent IDH^{WT} glioblastomas, we found that the vast majority of recurrent tumors regrew from multiple genetic subclones in the primary tumors, thus reflecting the existing heterogeneity at the time of resection. Our data contrast with the description by Kim et al. (2015) of divergent glioblastoma recurrences that share few genetic alterations with the primary tumor and originate from cells that branched off early during tumorigenesis. This was associated with regrowth of the tumor in a location distant from the original lesion. In our study, 90% of the tumors regrew in the same location as the primary tumor. Therefore, the common pattern of clonal evolution identified here may be characteristic of locally regrowing glioblastomas.

Our findings imply that standard therapy exerted little selective pressure on most recurrent tumors. Consistent with this idea, the vast majority of driver mutations were acquired prior to initial diagnosis and only few drivers were acquired after initial treatment, which contrasts with progressive evolution observed in low-grade glioma (Johnson et al., 2014) and indicates that IDH^{WT} glioblastomas attained their full aggressiveness already before initial diagnosis. Indeed, we uncovered a common path of early tumorigenesis among our cohort: all tumors harbored at least one clonal copy number change in *EGFR* (gain of chromosome 7), *CDKN2A/B* (loss of chromosome 9p or focal deletion), or *PTEN* (loss of chromosome 10/10q, with one tumor having a *PTEN* mutation instead of a loss), which is consistent with the overall abundance of these events in the respective TCGA cohort (Brennan et al., 2013; Grossman et al., 2016) and further studies (Sottoriva et al., 2013; Gerstung et al., 2017; Ozawa et al., 2014; Brastianos et al., 2017). The observation that clonal 9p loss/focal deletion of *CDKN2A/B* always occurred in conjunction with chromosome 7 gain or 10/10q loss indicates that the former does not take place before the latter.

While it has been suggested that *TERT* promoter mutations are very early events in IDH^{WT} glioblastomas (Barthel et al., 2018), we found them to be subclonal in one-third of our cohort. This subclonal resolution places *TERT* promoter mutations at a subsequent stage of tumorigenesis (see also Juratli et al., 2017; Landa et al., 2016). However, as *TERT* promoter mutations occur in all tumors (except for one primary sample), they appear to be associated with a selective advantage. During treatment, two out of seven tumors with a subclonal VAF of the *TERT* promoter mutation progressed to clonality, but there was no overall increase in the respective VAFs that remained subclonal. Recent studies linking *TERT* promoter mutation to better response to alkylating chemotherapy in IDH^{WT} glioblastomas with *MGMT* promoter methylation (Arita et al., 2016; Nguyen et al., 2017) raise the question of how chemotherapy may modulate the abundance of subclones depending on their mutation spectrum.

Combining data on genetic evolution and tumor growth, we inferred that IDH^{WT} glioblastomas originated several years prior to diagnosis, which contrasts with reports of patients who had mild or no abnormalities in MRI scans but progressed to glioblastoma or high-grade glioma within several months (e.g., Nishi et al., 2009; Landy et al., 2000). However, our time estimate relies on the count of somatic mutations and hence starts from the undetectable cell of origin. Comparing the number of cell divisions needed to accumulate the observed mutation counts with tumor size indicates a high rate of tumor cell death, so that only a minor fraction of cell divisions supports tumor growth. Therefore, it is plausible that the tumor remains of undetectable or barely detectable size for several years. To grow above the detection limit of current imaging techniques (about a millimeter in diameter), the tumor may need to acquire further mutations that stabilize cell survival. Activating *TERT* promoter mutations are a paradigmatic example of such mutations (Chiba et al., 2017), and our finding of subclonality of *TERT* promoter mutations in a sizable fraction of tumors is consistent with the acquisition of this mutation in the process of tumor evolution.

ACKNOWLEDGMENTS

The authors would like to thank the staff at the clinical centers of the German Glioma Network for their support; Stephan Wolf and the DKFZ Genomics and Proteomics Core Facility for their support in whole-genome and RNA sequencing and for providing the Illumina Methylation Beadchips and related services; Jules Kerssemakers and the DKFZ Omics IT and Data Management Core Facility for their support in data processing and deposition at EGA. We thank Stefan Pusch and Daniel Schrimpf for supporting the analyses of 450k/EPIC methylation data. We are grateful to Nagarajan Paramasivam and Naveed Ishaque for support on calling and interpretation of small mutations and structural variants. Roland Eils, Hai-Kun Liu, Markus Löffler, and Stefan Pfister are acknowledged for discussions. This study was supported within the e:med program of the German Ministry of Education and Research (BMBF) by the collaborative research project "SYS-GLIO – Systems-based prediction of the biological and clinical behavior of gliomas" (coordinator: P.L.; grant no. 031A425). The German Glioma Network was funded from 2004 to 2012 by the German Cancer Aid (grant no. 70-3163-Wi 3). A.Z. had a Ph.D. grant from the Düsseldorf School of Oncology, Heinrich Heine University Düsseldorf, Germany. T.H. acknowledges support by the BMBF research project "SYSMED-NB" (grant no. 01ZX1307B). B.R. and P.L. thank the DKFZ-Heidelberg Center for Personalized Oncology (DKFZ-HIPO) for technical support and funding through HIPO_project H043.

AUTHOR CONTRIBUTIONS

V.K., G.R., T.H., and P.L. led the study and wrote the manuscript with input from all co-authors. V.K., M.Schlesner, and T.H. designed and supervised the bioinformatic analyses. V.K., J.Y., P.B., Z.G., D.H., and M.N.C.F. performed the bioinformatic analyses. V.K. and T.H. designed and performed the mathematical modeling. Y.W. generated RNA and whole-genome sequencing DNA sequencing data. D.S. and A.v.D. generated and evaluated DNA methylation data. A.Z., K.K., J.F., and G.R. generated and evaluated gene panel sequencing data. J.F. and G.R. performed the histological classification of tumor samples. J.F. and K.K. extracted nucleic acids and managed biobanking. D.J., B.R., and M.S. led and performed the RNA sequencing and whole-genome sequencing experiments, and performed data analyses. K.L., J.C.T., C.H.-M., G.S., M.Sabel, B.H., and M.W. provided the patient samples and associated clinical details that made the study possible. D.J., B.R., and M.W. gave valuable input regarding study design, data analysis, and interpretation of results. G.R., T.H., and P.L. provided financial and technical infrastructure, and served as joint senior authors and project co-leaders. All authors read and approved the final manuscript.

DECLARATION OF INTERESTS

G.R. received research grants from Roche and Merck (EMD, Darmstadt), and honoraria for advisory boards from AbbVie. M.W. received research grants from Acceleron, Actelion, Bayer, Isarna, Merck, Sharp & Dohme, Merck (EMD, Darmstadt), Novocure, OGD2, Piqur and Roche, as well as honoraria for lectures or advisory board participation or consulting from BMS, Celldex, Immunocellular Therapeutics, Isarna, Magforce, Merck, Sharp & Dohme, Merck (EMD, Darmstadt), Northwest Biotherapeutics, Novocure, Pfizer, Roche, Teva, and Tocagen. J.C.T. received research honoraria for lectures or advisory board participation or consulting from Celldex, Roche, Siemens and BrainLab. The other authors declare no conflicts of interest.

REFERENCES

Alexandrov, L.B., Nik-Zainal, S., Wedge, D.C., Aparicio, S.A., Behjati, S., Biankin, A.V., Bignell, G.R., Bolli, N., Borg, A., Børresen-Dale, A.L., et al. (2013). Signatures of mutational processes in human cancer. Nature *22*, 415–421.

Anders, S., Pyl, P.T., and Huber, W. (2015). HTSeq—a Python framework to work with high-throughput sequencing data. Bioinformatics *31*, 166–169.

Arita, H., Yamasaki, K., Matsushita, Y., Nakamura, T., Shimokawa, A., Takami, H., Tanaka, S., Mukasa, A., Shirahata, M., Shimizu, S., et al. (2016). A combination of TERT promoter mutation and MGMT methylation status predicts clinically relevant subgroups of newly diagnosed glioblastomas. Acta Neuropathol. Commun. *4*, 79.

Aryee, M.J., Jaffe, A.E., Corrada-Bravo, H., Ladd-Acosta, C., Feinberg, A.P., Hansen, K.D., and Irizarry, R.A. (2014). Minfi: a flexible and comprehensive Bioconductor package for the analysis of Infinium DNA methylation microarrays. Bioinformatics *30*, 1363–1369.

Barthel, F.P., Wesseling, P., and Verhaak, R.G.W. (2018). Reconstructing the molecular life history of gliomas. Acta Neropathol. *135*, 649–670.

Becht, E., Giraldo, N.A., Lacroix, L., Buttard, B., Elarouci, N., Petitprez, F., Selves, J., Laurent-Puig, P., Sautès-Fridman, C., Fridman, W.H., et al. (2016). Estimating the population abundance of tissue-infiltrating immune and stromal cell populations using gene expression. Genome Biol. *17*, 218.

Bozic, I., Gerold, J.M., and Nowak, M.A. (2016). Quantifying clonal and subclonal passenger mutations in cancer evolution. PLoS Comput. Biol. *12*, e1004731.

Brastianos, P.K., Nayyar, N., Rosebrock, D., Leshchiner, I., Gill, C.M., Livitz, D., Bertalan, M.S., D'Andrea, M., Hoang, K., Aquilanti, E., et al. (2017). Resolving the phylogenetic origin of glioblastoma via multifocal genomic analysis of pre-treatment and treatment-resistant autopsy specimens. NPJ Precision Oncol. *33*, 1–33.

Brennan, C.W., Verhaak, R.G., McKenna, A., Campos, B., Noushmehr, H., Salama, S.R., Zheng, S., Chakravarty, D., Sanborn, J.Z., Berman, S.H., et al. (2013). The somatic genomic landscape of glioblastoma. Cell *155*, 462–477.

Capper, D., Jones, D.T.W., Sill, M., Hovestadt, V., Schrimpf, D., Sturm, D., Koelsche, C., Sahm, F., Chavez, L., Reuss, D.E., et al. (2018). DNA methylation-based classification of central nervous system tumours. Nature *22*, 469–474.

Chen, J., and Chen, Z. (2008). Extended Bayesian information criteria for model selection with large model spaces. Biometrika *95*, 759–771.

Cheng, Z., Li, Z., Ma, K., Li, X., Tian, N., Duan, J., Xiao, X., and Wang, Y. (2017). Long non-coding RNA XIST promotes glioma tumorigenicity and angiogenesis by acting as a molecular sponge of miR-429. J. Cancer *8*, 4106–4116.

Chiba, K., Lorbeer, F.K., Hunter Shain, A., McSwiggen, D.T., Schruf, E., Oh, A., Ryu, J., Darzacq, X., Bastian, B.C., and Hockemeyer, D. (2017). Mutations in the promoter of the telomerase gene *TERT* contribute to tumorigenesis by a two-step mechanism. Science *357*, 1416–1420.

deCarvalho, A.C., Kim, H., Poisson, L.M., Winn, M.E., Mueller, C., Cherba, D., Koeman, J., Seth, S., Protopopov, A., Felicella, M., et al. (2018). Discordant inheritance of chromosomal and extrachromosomal DNA elements contributes to dynamic disease evolution in glioblastoma. Nat. Genet. *50*, 708–717.

DeVita, V.T., Jr., Young, R.C., and Canellos, G.P. (1975). Combination versus single agent chemotherapy: a review of the basis for selection of drug treatment of cancer. Cancer *35*, 98–110.

Dobin, A., Davis, C.A., Schlesinger, F., Drenkow, J., Zaleski, C., Jha, S., Batut, P., Chaisson, M., and Gingeras, T.R. (2013). STAR: ultrafast universal RNA-seq aligner. Bioinformatics *29*, 15–21.

Drachman, D. (2005). Do we have brain to spare? Neurology *64*, 2004–2005.

Forbes, S.A., Beare, D., Boutselakis, H., Bamford, S., Bindal, N., Tate, J., Cole, C.G., Ward, S., Dawson, E., Ponting, L., et al. (2016). COSMIC: somatic cancer genetics at high-resolution. Nucleic Acids Res. *45*, D777–D783.

Francis, J.M., Zhang, C.Z., Maire, C.L., Jung, J., Manzo, V.E., Adalsteinsson, V.A., Homer, H., Haidar, S., Blumenstiel, B., Pedamallu, C.S., et al. (2014).

EGFR variant heterogeneity in glioblastoma resolved through single-nucleus sequencing. Cancer Discov. *4*, 956–971.

Gerlinger, M., and Swanton, C. (2010). How Darwinian models inform therapeutic failure initiated by clonal heterogeneity in cancer medicine. BJC *103*, 1139–1143.

Gerstung, M., Jolly, C., Leshchiner, I., Dentro, S.C., Gonzalez, S., Mitchell, T.J., Rubanova, Y., Anur, P., Rosebrock, D., Yu, K., et al. (2017). The evolutionary history of 2,658 cancers. BioRxiv, 161562, Available from: https://doi.org/10.1101/161562

Giessler, K.M., Kleinheinz, K., Huebschmann, D., Balasubramanian, G.P., Dubash, T.D., Dieter, S.M., Siegl, C., Herbst, F., Weber, S., Hoffmann, C.M., et al. (2017). Genetic subclone architecture of tumor clone-initiating cells in colorectal cancer. J. Exp. Med. *214*, 2073–2088.

Goldberg-Zimring, D., Talos, I.F., Bhagwat, J.G., Haker, S.J., Black, P.M., and Zou, K.H. (2005). Statistical validation of brain tumor shape approximation via spherical harmonics for image-guided neurosurgery. Acad. Radiol. *12*, 459–466.

Gonzalez-Perez, A., Perez-Llamas, C., Deu-Pons, J., Tamborero, D., Schroeder, M.P., Jene-Sanz, A., Santos, A., and Lopez-Bigas, N. (2013). IntOGen-mutations identifies cancer. Nat. Methods *10*, 1081–1082.

Greaves, M., and Maley, C.C. (2012). Clonal evolution in cancer. Nature *481*, 306–313.

Gröbner, S.N., Worst, B.C., Weischenfeldt, J., Buchhalter, I., Kleinheinz, K., Rudneva, V.A., Johann, P.D., Balasubramanian, G.P., Segura-Wang, M., Brabetz, S., et al. (2018). The landscape of genomic alterations across childhood cancers. Nature *555*, 321–327.

Grossman, R.L., Heath, A.P., Ferretti, V., Varmus, H.E., Lowy, D.R., Kibbe, W.A., and Staudt, L.M. (2016). Toward a shared vision for cancer genomic data. N. Engl. J. Med. *375*, 1109–1112.

Hegi, M.E., Diserens, A.C., Gorlia, T., Hamou, M.F., de Tribolet, N., Weller, M., Kros, J.M., Hainfellner, J.A., Mason, W., Mariani, L., et al. (2005). MGMT gene silencing and benefit from temozolomide in glioblastoma. N. Engl. J. Med. *352*, 997–1003.

Herculaono-Houzel, S., Mota, B., and Lent, R. (2006). Cellular scaling rules for rodent brains. Proc. Natl. Acad. Sci. U S A *103*, 12138–12143.

Hu, L.S., Ning, S., Eschbacher, J.M., Baxter, L.C., Gaw, N., Ranjbar, S., Plasencia, J., Dueck, A.C., Peng, S., Smith, K.A., et al. (2017). Radiogenomics to characterize regional genetic heterogeneity in glioblastoma. Neuro Oncol. *19*, 128–137.

Huebschmann, D., Gu, Z., and Schlesner, M. (2015). YAPSA: yet another package for signature analysis, Available from: https://bioconductor.org/packages/devel/bioc/html/YAPSA.html

Jaffe, A.E. (2018). FlowSorted.Blood.450k: Illumina HumanMethylation data on sorted blood cell populations, Available from: https://www.bioconductor.org/packages/release/data/experiment/html/FlowSorted.Blood.450k.html

Jaffe, A.E., and Kaminsky, Z.A. (2018). FlowSorted.DLPFC.450k: Illumina HumanMethylation data on sorted frontal cortex cell populations, Available from: https://bioconductor.org/packages/release/data/experiment/html/FlowSorted.DLPFC.450k.html

Jin, N., Yang, L.Y., and Xu, Z.P. (2017). Long non-coding RNA HOTTIP is able to predict poor prognosis in various neoplasms: a meta-analysis. Mol. Clin. Oncol. *7*, 263–266.

Johnson, B.E., Mazor, T., Hong, C., Barnes, M., Aihara, K., McLean, C.Y., Fouse, S.D., Yamamoto, S., Ueda, H., Tatsuno, K., et al. (2014). Mutational analysis reveals the origin and therapy-driven evolution of recurrent glioma. Science *343*, 189–193.

Juratli, T.A., Thiede, C., Koerner, M.V.A., Tummala, S.S., Daubner, D., Shankar, G.M., Williams, E.A., Martinez-Lage, M., Soucek, S., Robel, K., et al. (2017). Intratumoral heterogeneity and TERT promoter mutations in progressive/higher-grade meningiomas. Oncotarget *8*, 109228–109237.

Khan, A., and Zhang, X. (2016). dbSUPER: a database of super-enhancers in mouse and human genome. Nucleic Acids Res. *44*, D164–D171.

Kim, H., Zheng, S., Amini, S.S., Virk, S.M., Mikkelsen, T., Brat, D.J., Grimsby, J., Sougnez, C., Muller, F., Hu, J., et al. (2015). Whole-genome and multisector exome sequencing of primary and post-treatment glioblastoma reveals patterns of tumor evolution. Genome Res. *3*, 316–327.

Kimura, M. (1969). The number of heterozygous nucleotide sites maintained in a finite population due to steady flux of mutations. Genetics *61*, 893–903.

Kleinheinz, K., Bludau, I., Hübschmann, D., Heinold, M., Kensche, P., Gu, Z., López, C., Hummel, M., Klapper, W., Möller, P., et al. (2017). ACEseq-allele specific copy number estimation from whole genome sequencing. BioRxiv, 210807, Available from: https://doi.org/10.1101/210807

Landa, I., Ibrahimpasic, T., Boucai, L., Sinha, R., Knauf, J.A., Shah, R.H., Dogan, S., Ricarte-Filho, J.C., Krishnamoorthy, G.P., Xu, B., et al. (2016). Genomic and transcriptomic hallmarks of poorly differentiated and anaplastic thyroid cancers. J. Clin. Invest. *126*, 1052–1066.

Landy, H.J., Lee, T.T., Potter, P., Feun, L., and Markoe, A. (2000). Early MRI findings in high grade glioma. J. Neurooncol. *47*, 65–72.

Li, H., and Durbin, R. (2009). Fast and accurate short read alignment with Burrows-Wheeler transform. Bioinformatics *25*, 1754–1760.

Li, H., Handsaker, B., Wysoker, A., Fennell, T., Ruan, J., Homer, N., Marth, G., Abecasis, G., and Durbin, R.; 1000 Genome Project Data Processing Subgroup (2009). The sequence alignment/map format and SAMtools. Bioinformatics *25*, 2078–2079.

Ling, S., Hu, Z., Yang, Z., Yang, F., Li, Y., Lin, P., Chen, K., Dong, L., Cao, L., Tao, Y., et al. (2015). Extremely high genetic diversity in a single tumor points to prevalence of non-Darwinian cell evolution. Proc. Natl. Acad. Sci. U S A *112*, E6496–E6505.

Louis, D.N., Perry, A., Reifenberger, G., von Deimling, A., Figarella-Branger, D., Cavanee, W.K., Ohgaki, H., Wiestler, O.D., Kleihues, P., and Ellison, D.W. (2016). The 2016 World Health Organization classification of tumors of the central nervous system: a summary. Acta Neuropathol. *131*, 803–820.

Love, M.I., Huber, W., and Anders, S. (2014). Moderated estimation of fold change and dispersion for RNA-seq data with DESeq2. Genome Biol. *15*, 550.

Meyer, M., Reimand, J., Lan, X., Head, R., Zhu, X., Kushida, M., Bayani, J., Pressey, J.C., Lionel, A.C., Clarke, I.D., et al. (2013). Single-cell derived clonal analysis of human glioblastoma links functional and genomic heterogeneity. Proc. Natl. Acad. Sci. U S A *112*, 851–856.

Milholland, B., Dong, X., Zhang, L., Hao, X., Suh, Y., and Vijg, J. (2017). Differences between germline and somatic mutation rates in humans and mice. Nat. Commun. *8*, 15183.

Milo, R., Jorgensen, P., Moran, U., Weber, G., and Springer, M. (2010). BioNumbers—the database of key numbers in molecular and cell biology. Nucleic Acids Res. *38*, D750–D753.

Del Monte, U. (2009). Does the cell number 10(9) still really fit one gram of tumor tissue? Cell Cycle *8*, 505–506.

Mularoni, L., Sabarinathan, R., Deu-Pons, J., Gonzalez-Perez, A., and López-Bigas, N. (2016). OncodriveFML: a general framework to identify coding and non-coding regions with cancer driver mutations. Genome Biol. *17*, 128.

Nathanson, D.A., Gini, B., Mottahedeh, J., Visnyei, K., Koga, T., Gomez, G., Eskin, A., Hwang, K., Wang, J., Masui, K., et al. (2014). Targeted therapy resistance mediated by dynamic regulation of extrachromosomal mutant EGFR DNA. Science *343*, 72–76.

Nguyen, H.N., Lie, A., Li, T., Chowdhury, R., Liu, F., Ozer, B., Wei, B., Green, R.M., Ellingson, B.M., Wang, H.J., et al. (2017). Human TERT promoter mutation enables survival advantage from MGMT promoter methylation in IDH1 wild-type primary glioblastoma treated by standard chemoradiotherapy. Neuro Oncol. *19*, 394–404.

Nishi, N., Kawai, S., Yonezawa, T., Fujimoto, K., and Masui, K. (2009). Early appearance of high grade glioma on magnetic resonance imaging. Neurol. Med. Chir. (Tokyo) *49*, 8–12.

Ostrom, Q.T., Gittleman, H., Xu, J., Kromer, C., Wolinsky, Y., Kruchko, C., and Barnholtz-Sloan, J.S. (2016). Primary brain and other central nervous system tumors diagnosed in the United States in 2009–2013. Neuro Oncol. *18*, v1–v75.

Ozawa, T., Riester, M., Cheng, Y.-K., Huse, J.T., Squatrito, M., Helmy, K., Charles, N., Michor, F., and Holland, E.C. (2014). Most human non-GCIMP glioblastoma subtypes evolve from a common proneural-like precursor glioma. Cancer Cell *26*, 288–300.

Pakkenberg, B., Gundersen, H.J., Mortensen, E.L., Lauritzen, M.J., Jeune, B., Regeur, L., West, M.J., and Schwartz, T.W. (1997). The normal brain: a new knowledge in different fields. Ugeskr Laeger *159*, 723–727.

Patel, A.P., Tirosh, I., Trombetta, J.J., Shalek, A.K., Gillespie, S.M., Wakimoto, H., Cahill, D.P., Nahed, B.V., Curry, W.T., Martuza, R.L., et al. (2014). Single-cell RNA-seq highlights intratumoral heterogeneity in primary glioblastoma. Science *344*, 1396–1401.

Qazi, M.A., Vora, P., Venugopal, C., Sidhu, S.S., Moffat, J., Swanton, C., and Singh, S.K. (2017). Intratumoral heterogeneity: pathways to treatment resistance and relapse in human glioblastoma. Ann. Oncol. *28*, 1448–1456.

R Core Team (2017). R: A Language and Environment for Statistical Computing (R Foundation for Statistical Computing), Available from: https://www.R-project.org/

Rimmer, A., Phan, H., Mathieson, I., Iqbal, Z., Twigg, S.R.F., WGS500 Consortium, Wilkie, A.O.M., McVean, G., and Lunter, G. (2014). Integrating mapping-, assembly- and haplotype-based approaches for calling variants in clinical sequencing applications. Nat. Genet. *46*, 1–9.

Rubio-Perez, C., Tamborero, D., Schroeder, M.P., Antolín, A.A., Deu-Pons, J., Perez-Llamas, C., Mestres, J., Gonzalez-Perez, A., and Lopez-Bigas, N. (2015). In silico prescription of anticancer drugs to cohorts of 28 tumor types reveals novel targeting opportunities. Cancer Cell *27*, 382–396.

Sherry, S.T., Ward, M.H., Kholodov, M., Baker, J., Phan, L., Smigielski, E.M., and Sirotkin, K. (2001). dbSNP: the NCBI database of genetic variation. Nucleic Acids Res. *29*, 308–311.

Snuderl, M., Fazlollahi, L., Le, L.P., Nitta, M., Zhelyazkova, B.H., Davidson, C.J., Akhavanfard, S., Cahill, D.P., Aldape, K.D., Betensky, R.A., et al. (2011). Mosaic amplification of multiple receptor tyrosine kinase genes in glioblastoma. Cancer Cell *20*, 810–817.

Sottoriva, A., Spiteri, I., Piccirillo, S.G.M., Touloumis, A., Collins, V.P., Marioni, J.C., Curtis, C., Watts, C., and Tavaré, S. (2013). Intratumor heterogeneity in human glioblastoma reflects cancer evolutionary dynamics. Proc. Natl. Acad. Sci. U S A *110*, 4009–4014.

Sturm, D., Witt, H., Hovestadt, V., Khuong-Quang, D.A., Jones, D.T., Konermann, C., Pfaff, E., Tönjes, M., Sill, M., Bender, S., et al. (2012). Hotspot mutations in H3F3A and IDH1 define distinct epigenetic and biological subgroups of glioblastoma. Cancer Cell *22*, 425–437.

Tischler, G., and Leonard, S. (2014). biobambam: tools for read pair collation based algorithms on BAM files. Source Code Biol. Med. *9*, 1–18.

Wang, K., Li, M., and Hakonarson, H. (2010). ANNOVAR: functional annotation of genetic variants from high-throughput sequencing data. Nucleic Acids Res. *38*, 1–7.

Wang, J., Cazzato, E., Ladewig, E., Frattini, V., Rosenbloom, D.I., Zairis, S., Abate, F., Liu, Z., Elliott, O., Shin, Y.J., et al. (2016). Clonal evolution of glioblastoma under therapy. Nat. Genet. *48*, 768–776.

Wang, Q., Hu, B., Hu, X., Kim, H., Squatrito, M., Scarpace, L., deCarvalho, A.C., Lyu, S., Li, P., Li, Y., et al. (2017). Tumor evolution of glioma-intrinsic gene expression subtypes associates with immunological changes in the microenvironment. Cancer Cell *32*, 42–56.

Wang, Q., Teng, Y., Wang, R., Deng, D., You, Y., Peng, Y., Shao, N., and Zhi, F. (2018). The long non-coding RNA SNHG14 inhibits cell proliferation and invasion and promotes apoptosis by sponging miR-92a-3p in glioma. Oncotarget *9*, 12112–12124.

Weller, M., van den Bent, M., Tonn, J.C., Stupp, R., Preusser, M., Cohen-Jonathan-Moyal, E., Henriksson, R., Le Rhun, E., Balana, C., Chinot, O., et al. (2017). European Association for Neuro-Oncology (EANO) guideline on the diagnosis and treatment of adult astrocytic and oligodendroglial gliomas. Lancet Oncol. *18*, e315–329.

Williams, M.J., Werner, B., Barnes, C.P., Graham, T.A., and Sottoriva, A. (2016). Identification of neutral tumor evolution across cancer types. Nat. Genet. *48*, 238–244.

Yao, Y., Ma, J., Xue, Y., Wang, P., Li, Z., Liu, J., Chen, L., Xi, Z., Teng, H., Wang, Z., et al. (2015). Knockdown of long non-coding RNA XIST exerts tumor-suppressive functions in human glioblastoma stem cells by up-regulating miR-152. Cancer Lett. *359*, 75–86.

Zacher, A., Kaulich, K., Stepanow, S., Wolter, M., Köhrer, K., Felsberg, J., Malzkorn, B., and Reifenberger, G. (2017). Molecular diagnostics of gliomas using next generation sequencing of a glioma-tailored gene panel. Brain Pathol. *27*, 146–159.

STAR METHODS

KEY RESOURCES TABLE

REAGENT or RESOURCE	SOURCE	IDENTIFIER
Antibodies		
Mouse monoclonal anti-ATRX (clone AX1)	Dianova	Cat#DIA-AX1
Critical Commercial Assays		
JETQUICK Tissue DNA Spin Kit	Genomed	Cat#440250
Pure Link Genomic DNA Mini Kit	Invitrogen	Cat#K-182001
RNeasy Mini Kit	Qiagen	Cat#74104
GeneRead DNA FFPE Kit	Qiagen	Cat#180134
TruSeq DNA Nano	Illumina	Cat# 20015965
HiSeq X Ten Reagent Kit v2.5	Illumina	Cat# FC-501-2501
TruSeq Stranded Total RNA LT Sample Prep Kit	Illumina	RS–122-2201
Ion AmpliSeq™ Library 2.0 Kit	Life Technologies	Cat#4480441
PI™ Template OT2 200 Kit v3	Life Technologies	Cat#4488318
Ion PI™ 200 Sequencing 200 Kit v3	Life Technologies	Cat#4488315
Deposited Data		
Panel sequenced DNA	This paper	European Genome-phenome Archive (EGA): EGAD00001004565, EGAS00001003184
WGS data	This paper	European Genome-phenome Archive (EGA): EGAD00001004563, EGAS00001003184
RNA sequencing data	This paper	European Genome-phenome Archive (EGA): EGAD00001004564, EGAS00001003184
450k/EPIC methylation data	This paper	European Genome-phenome Archive (EGA): EGAD00010001642, EGAD00010001643, EGAS00001003184
FlowSorted.DLPFC.450k	Jaffe and Kaminsky, 2018	https://bioconductor.org/packages/release/data/experiment/html/FlowSorted.DLPFC.450k.html
FlowSorted.Blood.450k	Jaffe, 2018	http://bioconductor.org/packages/release/data/experiment/html/FlowSorted.Blood.450k.html
Genomic coordinates of coding regions	Mularoni et al., 2016	https://bitbucket.org/bbglab/oncodrivefml/downloads/
Genomic coordinates of putatively functional non-coding regions	Lesurf et al., 2016	http://www.oreganno.org/dump/ORegAnno_Combined_2016.01.19.tsv
Software and Algorithms		
Torrent Suite™ software 4.4	Life Technologies	https://www.thermofisher.com/
Integrative Genomics Viewer	Robinson et al., 2011 and Thorvaldsdóttir et al., 2013	https://software.broadinstitute.org/software/igv/
NextGENe® v.2.3.4	SoftGenetics	https://softgenetics.com/NextGENe.php
bwa mem version 0.7.8	Li and Durbin, 2009	https://sourceforge.net/projects/bio-bwa/files/
biobambam version 0.0.148	Tischler and Leonard, 2014	https://github.com/gt1/biobambam/releases
DKFZ core variant calling workflows	German Cancer Research Center	https://dockstore.org/containers/quay.io/pancancer/pcawg-dkfz-workflow
samtools	Li et al., 2009	https://sourceforge.net/projects/samtools/files/samtools/
Bcftools version 0.1.19	Li et al., 2009	https://samtools.github.io/bcftools/
Platypus	Rimmer et al., 2014	https://github.com/andyrimmer/Platypus
ANNOVAR	Wang et al., 2010	annovar.openbioinformatics.org/en/la…
SOPHIA v.34.0	In-house	https://bitbucket.org/utoprak/sophia
ACEseq	Kleinheinz et al., 2017	https://aceseq.readthedocs.io/en/latest/

(*Continued on next page*)

Continued		
REAGENT or RESOURCE	SOURCE	IDENTIFIER
STAR v2.3.0e	Dobin et al., 2013	https://github.com/alexdobin/STAR
htseq-count v0.6.0	Anders et al., 2015	https://htseq.readthedocs.io/en/master/count.html
Classification using methylation profiling	Capper et al., 2018	https://www.molecularneuropathology.org/mnp
R package YAPSA	Huebschmann et al., 2015	http://bioconductor.org/packages/release/bioc/html/YAPSA.html
R package MCP-counter	Becht et al., 2016	https://github.com/ebecht/MCPcounter
R package minfi	Aryee et al., 2014	https://bioconductor.org/packages/release/bioc/html/minfi.html
R package DESeq2	Love et al., 2014	https://bioconductor.org/packages/release/bioc/html/DESeq2.html
OncodriveFML	Mularoni et al., 2016	https://oncodrivefml.readthedocs.io/en/latest/workflow.html
R scripts for phylogenetic inference and modeling of clonal dynamics	This paper	Data S1; https://github.com/hoefer-lab/phy_clo_dy
Other		
Gene panel 1	Zacher et al., 2017	https://onlinelibrary.wiley.com/doi/epdf/10.1111/bpa.12367
Gene panel 2	This paper	STAR Methods, 'Gene panel and next generation sequencing'
Ion AmpliSeq™ DNA and RNA Library Preparation	Life Technologies	MAN0006735 Rev 5.0

CONTACT FOR REAGENT AND RESOURCE SHARING

Further information and requests for resources and reagents should be directed to and will be fulfilled by the Lead Contact, Peter Lichter (peter.lichter@dkfz.de).

EXPERIMENTAL MODEL AND SUBJECT DETAILS

Patients and Tissue Samples

We collected matched tissue samples from the initial surgery before treatment and a second surgery for recurrent tumor growth from 50 patients with IDH^{WT} glioblastoma, World Health Organization (WHO) grade IV. The patients were identified in the central database of the German Glioma Network (GGN) or the database of the Central Nervous System (CNS) tumor tissue bank at the Department of Neuropathology, Heinrich Heine University, Düsseldorf, Germany. The GGN is a prospective, non-interventional cohort study involving eight clinical centers at University Hospitals in Germany (www.gliomnetzwerk.de), and was supported by the German Cancer Aid from 2004 to 2012. Patients provided their written informed consent for participating in the GGN and the use of their tissue samples and clinical data for research purposes according to the research proposals approved by the Institutional Review Boards of the participating institutions. The present study was approved by the institutional review board of the Medical Faculty, Heinrich Heine University, Düsseldorf, Germany (study number 4940). Histology of all tumors was centrally reviewed and confirmed to correspond to glioblastoma, IDH^{WT}, World Health Organization (WHO) grade IV according to the WHO classification of central nervous system tumors 2016 (Louis et al., 2016). All tissue specimens used in the present study for extraction of nucleic acids and molecular analyses were histologically evaluated to assure that they consisted of vital tumor tissue. Tissue samples corresponding mostly to necrosis or reactive changes were excluded. Relevant clinical data retrieved for each patient included information on age at diagnosis, gender, tumor location, extent of resection, postoperative therapy, interval between primary and secondary surgery, and overall survival. Table S1 shows a summary of the respective patient data.

METHOD DETAILS

Immunohistochemical Stainings

Immunohistochemical stainings for ATRX (alpha-thalassemia/mental retardation syndrome, X-linked) protein expression were performed on representative formalin-fixed and paraffin-embedded tissue sections from selected cases of primary and recurrent tumors using an automated immunostainer (Dako, Kopenhagen, Denmark) and the UltraVision™ Quanto horseradish peroxidase detection system with 3,3'-diaminobenzidine tetrahydrochloride as chromogen (Thermo Fisher Scientific, Freemont, CA). Sections were pretreated by heating them in retrieval solution (Dako) at pH 9.0 for 20 min. As primary anti-ATRX antibody, we used the mouse

monoclonal IgG1 clone AX1 diluted 1:200 as recommended by the manufacturer (Dianova, Hamburg, Germany). All immunohistochemical sections were counterstained with hematoxylin.

Extraction of DNA and RNA

DNA was extracted from deep-frozen tumor tissue samples from 35 patients, including all patients whose tissue samples were subjected to WGS with the JETQUICK Tissue DNA Spin Kit (Genomed, Loehne, Germany). Extraction of constitutional (leukocyte) DNA from frozen peripheral blood samples was performed with the Pure Link Genomic DNA Mini Kit (Invitrogen, Carlsbad, CA). The RNeasy Mini Kit (Qiagen, Hilden, Germany) was used for extraction of total RNA from deep-frozen tissue samples. The GeneRead DNA FFPE Kit (Qiagen) was used for DNA extraction from formalin-fixed and paraffin-embedded (FFPE) samples of 15 patients whose tumor samples were subjected to panel sequencing. All nucleic acid extractions were carried out according to the respective kit manufacturer's protocol. Quality of extracted DNA was assured by spectrophotometric analysis and agarose gel electrophoresis. RNA quality was determined on an Agilent 2100 Bioanalyzer (Agilent Technologies, Santa Clara, CA). Only samples showing a RNA integrity number (RIN) of 6.5 or more were used for RNA sequencing.

DNA and RNA Library Preparation

DNA libraries were prepared according to the Illumina TruSeq Nano DNA Library protocol using the TruSeq DNA Nano kit (Illumina, Hayward, CA) and sequenced on HiSeq X using the HiSeq X Ten Reagent Kit v2.5 (both Illumina, Hayward, CA). Total, strand-specific RNA libraries were prepared according to the Illumina TruSeq Stranded Total RNA Sample Preparation Guide (Illumina, Hayward, CA), with Ribo Zero Gold (Epicentre, Madison, WI) depletion of rRNA.

Gene Panel Next Generation Sequencing

In total, we analyzed pairs of primary and recurrent IDH^{WT} glioblastomas from 43 patients (including 14 of the 21 patients whose tumors were analyzed by whole genome sequencing) using next generation sequencing of a gene panel covering 50 selected genes. Libraries for gene panel sequencing were prepared using the Ion AmpliSeq™ Library 2.0 Kit (Life Technologies, Carlsbad, CA, USA) and two customized AmpliSeq™ gene panels. Gene panel 1 has been published elsewhere (Zacher et al., 2017) and covers the complete coding sequences (cds) or selected genomic regions including mutation hot spots (region) of the following 20 genes: *NRAS* (cds), *FUBP1* (cds), *CDKN2C* (cds), *H3F3A* (region), *IDH1* (region), *PIK3CA* (cds), *TERT* (region), *PIK3R1* (cds), *EGFR* (cds), *BRAF* (region), *CDKN2A* (cds), *CDKN2B* (cds), *PTEN* (cds), *RB1* (cds), *IDH2* (region), *TP53* (cds), *NF1* (cds), *CIC* (cds), *NF2* (cds) and *ATRX* (cds). Gene panel 2 covers complete cds or regions including mutation hot spots of the following 30 genes: *MDM4* (region), *PIK3C2B* (cds), *ACVR1* (region), *MSH6* (cds), *MSH2* (cds), *RAB7A* (region), *MLH1* (cds), *PDGFRA* (cds), *MYB* (region), *CCND3* (region), *DAXX* (cds), *HIST1H3B* (cds), *CDK6* (region), *MET* (region), *PMS2* (cds), *MYBL1* (region), *FGFR1* (region), *NTRK2* (cds), *TSC1* (cds), *MTAP* (cds), *CCND1* (region), *CDK4* (region), *PTPN11* (cds), *MDM2* (region), *CCND2* (region), *KRAS* (cds), *IRS2* (region), *GABRG3* (region), *TSC2* (cds) and *PPM1D* (cds). Library preparation for gene panel sequencing was carried out according to the manufacturer's protocol (Zacher et al., 2017) (MAN 006735 Rev 5.0, Life Technologies). A total of four primer pools were PCR amplified using 10 ng of genomic DNA per primer pool as template. Emulsion PCR and enrichment was carried out on the Ion OneTouch™ 2 System using the Ion PI™ Template OT2 200 Kit v3 (MAN0009133 Rev A, Life Technologies). The Ion Proton™ System (Life Technologies) was used for sequencing using the Ion PI™v2 chips and the Ion PI™ 200 Sequencing 200 Kit v3 (MAN0009136 Rev.A, Life Technologies). Overall, at least 1 million reads were generated per library. Data analysis was performed with the Torrent Suite™ software 4.4 employing the implemented TMAP algorithm (Life Technologies). Variants were detected using the VariantCaller Plugin v4.4 and the predefined parameter set 'somatic high stringency' (Life Technologies, for detailed annotation information see Zacher et al., 2017). The Integrative Genomics Viewer (IGV) software was used to visualize the read alignment and check for possible errors. Copy number variations were identified with the NextGENe® v.2.3.4 software (SoftGenetics, State College, PA).

Alignment of Whole Genome Sequencing Reads

Read pairs were mapped to the human reference genome (build 37, version hs37d5) using bwa mem (Li and Durbin, 2009) (version 0.7.8, with minimum base quality threshold zero [-T 0] and remaining settings left at default values), followed by coordinate-sorting with bamsort (with compression option set to fast (1)) and marking duplicate read pairs with bammarkduplicates (with compression option set to (9)); both are part of biobambam (Tischler and Leonard, 2014) package version 0.0.148.

Detection of SNVs and Indels

Somatic SNVs and indels in matched tumor normal pairs were identified using the DKFZ core variant calling workflows of the ICGC PCAWG project (https://dockstore.org/containers/quay.io/pancancer/pcawg-dkfz-workflow). Briefly, in the DKFZ SNV pipeline candidate SNV calls were generated by samtools (Li et al., 2009) and bcftools (version 0.1.19), and potential variants called in the tumor were followed by a lookup of the corresponding positions in the control. To enable calling of variants with low allele frequency we disabled the Bayesian model (by setting -p 2). Thus, all positions containing at least one high quality non-reference base are reported as candidate variant. The resulting raw calls were categorized into putative somatic variants and others (artifacts, germline) based on the presence of variant reads in the matched normal sample. The frequency of all putative somatic variants was then refined by checking for potential redundant information due to overlapping reads, and precise base counts for each strand were determined. All variants were annotated with dbSNP141, 1000 Genomes (phase 1), Gencode Mapability track, UCSC High Seq Depth track,

UCSC Simple-Tandemrepeats, UCSC Repeat-Masker, DUKE-Excluded, DAC-Blacklist, UCSC Selfchain. The confidence for each variant was then determined by a heuristic scoring scheme taking the aforementioned tracks into account. In addition, variants with strong read biases which fell into a bias-prone context according to the strand bias filter were removed. High confidence variants (confidence score 8-10) were reported. For indel calling, Platypus (Rimmer et al., 2014) version 0.7.4 was used. All candidate indel variants were categorized into putative somatic and other based on the genotype likelihoods (matched genotype 0/0 for somatic indels). High confidence somatic variants were required to either have the Platypus filter flag PASS or pass custom filters allowing for low variant frequency using a scoring scheme. Candidates with the badReads flag, alleleBias, or strandBias were discarded if the variant allele frequency was <10%. Additionally, combinations of Platypus non-PASS filter flags, bad quality values, low genotype quality, very low variant counts in the tumor, and presence of variant reads in the control were not tolerated. SNVs and indels were annotated using ANNOVAR (Wang et al., 2010) according to GENCODE gene annotation (version 19) and overlapped with variants from dbSNP (Sherry et al., 2001) (build 141) and the 1000 Genomes Project database.

Detection of Structural Variants (SVs)

Genomic structural rearrangements were detected using SOPHIA v.34. Briefly, SOPHIA uses supplementary alignments as produced by bwa mem as indicators of a possible underlying SV. SV candidates are filtered by comparing them to a background control set of sequencing data (obtained using normal blood samples from a background population database of 3261 patients from published TCGA and ICGC studies and both published and unpublished DKFZ studies, sequenced using Illumina HiSeq 2000, 2500 (100 bp) and HiSeq X (151 bp) platforms and aligned uniformly using the same workflow as in this study). An SV candidate is discarded if (i) it has more than 85% of read support from low quality reads; (ii) the second breakpoint of the SV was unmappable in the sample and the first breakpoint was detected in 10 or more background control samples; (iii) an SV with two identified breakpoints had one breakpoint present in at least 98 control samples (3% of the control samples); or (iv) both breakpoints have less than 5% read support. SVs were annotated as somatic if the respective event had no support in the matched normal sample.

Detection of Copy Number Aberrations

Allele-specific copy-number aberrations were detected using ACEseq (allele-specific copy-number estimation from whole genome sequencing) (Kleinheinz et al., 2017). ACEseq determines absolute allele-specific copy numbers as well as tumor ploidy and tumor cell content based on coverage ratios of tumor and control as well as the B-allele frequency (BAF) of heterozygous single nucleotide polymorphisms (SNPs). SVs called by SOPHIA were incorporated to improve genome segmentation. The estimated tumor cell content was compared to the doubled median of the somatic SNV mutation allele frequency distribution and adjusted if the estimates deviated by more than 10% from each other. Genomic segments were annotated as losses if their total copy number (TCN) was smaller than the sample's ploidy by at least 0.3. Segments with an estimated TCN < 0.5 were annotated as homozygous deletions. Analogous to losses, gains were identified as segments with ploidy – TCN < -0.3. High level amplifications were classified as segments with TCN > 2.5 x ploidy. Loss of heterozygosity was defined as segments with the copy number of the minor allele < 0.3.

Alignment and Counting of RNA Sequencing Reads

Sequencing reads were aligned to the human genome (hg19 build) with the Gencode reference transcriptome (v19) using STAR (v2.3.0e) (Dobin et al., 2013). Read counts for each gene were determined as the total number of reads mapping to exons using htseq-count (0.6.0) (Anders et al., 2015) and the GENCODE transcript model (v19).

450k/EPIC Methylation Arrays

DNA methylation profiling was performed by using 450k or EPIC methylation bead arrays (Illumina, Hayward, CA) according to standard protocols. Data were processed and analysed as reported elsewhere (Capper et al., 2018).

Signature Analysis

Supervised mutational signature analysis was performed with the R package YAPSA (Huebschmann et al., 2015). Using the function LCD_complex_cutoff(), we computed a non-negative least squares (NNLS) decomposition of the mutational catalogue with 30 known signatures from COSMIC (http://cancer.sanger.ac.uk/cosmic/signatures)). In order to increase specificity, LCD_complex_cutoff() applies the NNLS algorithm twice. A first NNLS is run proposing all supplied signatures to the decomposition, then a second NNLS is run again with a reduced set of signatures consisting only of those signatures whose exposures were higher than a certain signature-specific cutoff. The signature-specific cutoffs were determined in a random operator characteristic (ROC) analysis using publicly available data on mutational catalogues of 7,042 cancer samples (507 from whole genome sequencing and 6,535 from whole exome sequencing; Alexandrov et al., 2013) and mutational signatures (http://cancer.sanger.ac.uk/cosmic/signatures, downloaded on January 15th, 2016). The following cut-offs were employed - AC1: 0; AC2: 0.03193533; AC3 0.1082812; AC4: 0.03266562; AC5: 0; AC6: 0.003351944; AC7: 0.0280924; AC8: 0.1814745; AC9: 0.09121354; AC10: 0.01686839; AC11: 0.07757047; AC12: 0.1937234; AC13: 0.01665886; AC14: 0.03158583; AC15: 0.03138468; AC16: 0.3521707; AC17: 0.004232865; AC18: 0.236441; AC19: 0.04058829; AC20: 0.04701714; AC21: 0.04009243; AC22: 0.03756267; AC23: 0.04005552; AC24: 0.03503163; AC25: 0.01658311; AC26: 0.0261603; AC27: 0.02200583; AC28: 0.03145322; AC29: 0.07188295; AC30: 0.03147694. This analysis was performed separately for hypermutated and non-hypermutated tumors. To identify signature enrichment and depletion patterns between shared and private, as well as between clonal and subclonal SNVs, a stratified signature analysis was performed using

the function run_SMC() from YAPSA as described in Giessler et al. (2017). Briefly, the stratified analysis was performed as a multistep procedure: (1) a supervised analysis of mutational signatures was run without any stratification; (2) for every SNV in a sample, the stratum it belonged to was annotated; (3) for every stratum, a stratum-specific mutational catalog was built; and (4) a supervised NNLS (using lsei) with the constraint that the sum of exposures per stratum equals the exposures computed by the unstratified analysis was performed. Thereafter, enrichment and depletion patterns for all mutational signatures detected in step 1 were computed (Kruskal Wallis tests followed by pairwise posthoc Nemenyi tests corrected for multiple testing according to Benjamini and Hochberg (BH)) from the exposures in all strata with the help of the function stat_test_SMC().

Estimation of Cell Type Composition

The enrichment of different cell types in tumor samples was evaluated from gene expression and DNA methylation data. Gene expression data were analyzed using the R package MCP-counter (Becht et al., 2016) on normalized read counts (logarithmic reads per kilobase per million). MCP-counter quantifies the abundance of eight immune cell populations, endothelial cells and fibroblasts from transcriptomic markers unique to either of the cell types. For each cell type a score is computed using the log2 geometric mean of the corresponding markers. Signatures of neural and blood cells in DNA methylation data were deconvolved using the function estimateCellCounts() implemented in the R packages minfi (Aryee et al., 2014). The function uses regression calibration to estimate the proportions of NeuN+ and NeuN- cells (FlowSorted.DLPFC.450k; Jaffe and Kaminsky, 2018) and of different blood cells (FlowSorted.Blood.450k; Jaffe, 2018) from 450k/EPIC methylation data.

Driver Gene Selection

Putative driver mutations in glioblastoma were called based on the public database Intogen (Rubio-Perez et al., 2015; Gonzalez-Perez et al., 2013) and from recurrence. Among coding genes we searched for overrepresentation launching OncodriveFML (Mularoni et al., 2016) (with the coding regions file taken from https://bitbucket.org/bbglab/oncodrivefml/downloads/) and accepted genes at q-values $\leq$ 0.1 (Benjamini-Hochberg-corrected). We included non-coding genes if they were mutated in more than five patients. We in addition included *TERT* promoter mutations as likely drivers (Barthel et al., 2018), considering the region up to 2,500 base pairs upstream of the transcription start site.

Subclonality Test

To determine subclonality in Figure 3A we modeled mutation counts as a sampling result from a binomial distribution. If sampling from a diploid locus, the sampling probability of a clonal mutation is 0.5x*CCF*, where *CCF* denotes the cancer cell fraction. We determined *CCF* during phylogenetic inference as described in detail below. Loci of different copy number states shift the sampling probability non-trivially. We excluded these loci, requiring a (normalized) coverage ratio between 0.9 and 1.1, and in addition excluded mutations on male sex chromosomes. Subclonality was then assumed if the measured mutation counts fell below the 95%-quantile of a binomial distribution with sampling probability 0.5x*CCF*, i.e.

$$P\left(X \leq r^{\mathrm{mut}}\right) = \sum_{k=0}^{r^{\mathrm{mut}}} \binom{r^{\mathrm{ref}} + r^{\mathrm{mut}}}{r^{\mathrm{mut}}} (0.5 \times CCF)^{r^{\mathrm{mut}}} \times (1 - 0.5 \times CCF)^{r^{\mathrm{ref}}} < 0.05. \quad \text{(Equation 1)}$$

where r^{ref} and r^{mut} denote the measured reference and mutated reads of a SNV or small insertion/deletion. In case of loss of heterozygosity, Equation (1) is modified to

$$P\left(X \leq r^{\mathrm{mut}}\right) = \sum_{k=0}^{r^{\mathrm{mut}}} \binom{r^{\mathrm{ref}} + r^{\mathrm{mut}}}{r^{\mathrm{mut}}} (CCF)^{r^{\mathrm{mut}}} \times (1 - CCF)^{r^{\mathrm{ref}}} < 0.05. \quad \text{(Equation 2)}$$

We then used the classified mutations to estimate the number of subclonal mutations that appear clonal in a tumor sample due to incomplete tissue sampling. The fraction of these false positive clonal mutations can be assessed from mutations which were clonal in the primary and subclonal in the relapse sample. In fact, these mutations must have already been subclonal in the primary tumor as a transition from clonality to subclonality violates a single tumor origin. The false positive rate of clonal mutations due to incomplete tumor sampling thus reads

$$P(\text{subclonal in tumor} | \text{clonal in tumor sample}) = \frac{n_{\mathrm{cPsR}}}{n_{\mathrm{cPsR}} + n_{\mathrm{cPcR}}}, \quad \text{(Equation 3)}$$

where n_{cPsR} is the number of mutations which were clonal in the primary and subclonal in the relapse sample and n_{cPcR} is the number of mutations which were clonal in both samples.

Phylogenetic Inference

General Considerations

Our phylogenetic analysis aims at inferring genetic subclones in pairs of primary and relapse tumors that are characterized by a combination of oncogenic drivers (encompassing mutations and copy number variations). Thus we will deduce robust features of

the evolving phylogenetic tree of a tumor, including which driver mutations are in the common stem (i.e., occurred comparatively early) and which mutations are still subclonal at the times of surgical resection (and hence occurred later). Moreover, we will infer the common origins of subclones in the primary and relapse tumors, showing whether the relapse evolved from a unique subclone or multiple subclones in the primary tumor. For this analysis, we include all somatic variants specific to the tumor and do not restrict ourselves to known driver mutations. In particular, the majority of the 12,800 somatic SNVs recovered on average from a tumor are most likely neutral. However, the VAFs of neutral mutations in a tumor cell that harbors specific oncogenic drivers will grow in a coordinate manner as the subclone emerging from this cell expands, leading to many SNVs with the same VAF. In turn, this feature will facilitate the detection of the subclone in bulk WGS data.

The subclonal structure of a phylogenetic tree can be considered at different levels of resolution, from major branching down to single cells. Too fine a resolution is not of interest here because the vast majority of small subclones will be distinguished only by neutral somatic mutations that contain no information on tumor evolution by acquisition of driver mutations. Also, finely resolved phylogenetic trees cannot uniquely be reconstructed from bulk WGS data as mutations with small VAFs cannot be mapped uniquely to a large number of small subclones. These two considerations underscore our aim of reconstructing the occurrence of major drivers during genetic tumor evolution, which also motivates model selection (see below) favoring parsimonious trees that yield appropriate fits to the data. Importantly, the phylogenetic inference does not make assumptions on why two or more subclones coexist; coexistence could be a snapshot in the process of a newly evolved subclone outcompeting its predecessor(s) or be due to cooperation of subclones.

Assuming monoclonal origin of the tumor and neglecting the (very small) probability of backward evolution, a tumor can be visualized by a phylogenetic tree whose root corresponds to the founder cell of the tumor and whose tips represent the subclones in the tumor sample (Figure S3A). In accordance with the infinite sites hypothesis (Kimura, 1969), we assume that all SNVs and small insertions/deletions are singular events in the phylogenetic tree. Copy number changes often span larger regions so that the infinite sites model might not be adequate here, and a copy number change measured in both tumor samples could also be due to independent events. We address this by allowing up to two independent events changing copy number at a single locus, as described below in detail.

Mathematical Description of the Model

Assuming well-mixed samples, we model read counts in whole genome sequencing as a sampling result from a multinomial distribution, whose different categories represent the genetic subclones in the tumor. At each genomic locus the probability to sample reads from a distinct subclone scales with its relative size and its copy number state. Let $SC_i, i = \{1, \ldots, K\}$ denote the i-th subclone in a heterogeneous tumor with K subclones and $\mu = (\mu_1, \ldots, \mu_K)$ the proportion of cells in the sample originating from each subclone. Then, at each locus l, the probability to sample a read from SC_i in a Bernoulli trial can be written as

$$p_{i,l} = \mu_i \frac{\pi_{i,l}}{\sum_{i'=1}^{K} \mu_{i'} \pi_{i',l}} \quad \text{(Equation 4)}$$

where $\pi_l = (\pi_{1,l}, \ldots, \pi_{K,l})$ are integers that denote the copy numbers at locus l in each subclone. Now, let $s = (s_{1,l}, \ldots, s_{K,l} | s_{i,l} = \{0, \ldots, \pi_{i,l}\})$ be integers that denote the number of mutated alleles at locus l in each subclone. Accordingly, the probabilities to sample a read supporting the reference genome or a mutation, respectively, are given by

$$p_{i,l}^{\text{ref}} = p_{i,l}\left(1 - \frac{s_{i,l}}{\pi_{i,l}}\right) \quad \text{and} \quad p_{i,l}^{\text{mut}} = p_{i,l}\frac{s_{i,l}}{\pi_{i,l}}. \quad \text{(Equation 5)}$$

In bulk sequencing, the genomes from all subclones are intermingled. Consequently, r_L^{ref} reference reads and r_l^{mut} mutated reads at locus l originate from the K subclones in the sample, such that

$$r_l^{\text{ref}} = \sum_{i=1}^{K} r_{i,l}^{\text{ref}} \quad \text{and} \quad r_l^{\text{mut}} = \sum_{i=1}^{K} r_{i,l}^{\text{mut}}. \quad \text{(Equation 6)}$$

With this, the likelihood function for a measured number of reference and mutated reads at locus l is given by

$$\mathscr{L}_l\left(p_l \middle| r_l^{\text{ref}}, r_l^{\text{mut}}\right) = P_l\left(r_l^{\text{ref}}, r_l^{\text{mut}} \middle| p_l\right) = \frac{\left(r_l^{\text{ref}} + r_l^{\text{mut}}\right)!}{\prod_{i=1}^{K} r_{i,l}^{\text{ref}}! r_{i,l}^{\text{mut}}!} \prod_{i=1}^{K} \left(p_{i,l}^{\text{ref}}\right)^{r_{i,l}^{\text{ref}}} \left(p_{i,l}^{\text{mut}}\right)^{r_{i,l}^{\text{mut}}}, \quad \text{(Equation 7)}$$

with the corresponding log-likelihood, l_l,

$$l_l = \log \mathscr{L}_l = \mathscr{C} + \sum_{i=1}^{K} \left[r_{i,l}^{\text{ref}} \log\left(p_{i,l}^{\text{ref}}\right) + r_{i,l}^{\text{mut}} \log\left(p_{i,l}^{\text{mut}}\right)\right], \quad \text{(Equation 8)}$$

where C is a constant that solely depends on the read counts.

Solution Space and Phylogenetic Tree Design

We assume that tumors evolve from a monoclonal origin and can be visualized by a phylogenetic tree. This restricts the solution space for subclonal inference as we will see in the following. Invoking the infinite sites hypothesis (Kimura, 1969), we require that the combinations of subclones carrying a mutation can be explained by a single event in the tree and are present on one of the two parental alleles only. We thus require

$$0 \leq s_{i,l} \leq \max(B_{i,l}, \pi_{i,l} - B_{i,l}), \tag{Equation 9}$$

where $B_{i,l}$ is the number of B-alleles in the i-th subclone at locus l.

If an SNV collocates with a CNV, $s_{i,l}$ becomes further restricted by the following criteria:

- if the copy number change precedes the mutation in the phylogenetic tree, the mutation can only be present on one allele
- if the mutation precedes the copy number change, the mutation must either be present on all A-alleles or on all B-alleles
- if the order of mutation and copy number change is unclear, the mutation can be present on any number of A- or B-alleles.

Model Selection

To estimate μ, π and s, we first test a priori designed phylogenetic trees (Figure S3A). By treating normal tissue as an additional subclone, this automatically accounts for sample purity. Note that we designed the candidate trees in such a way that, in general, all subclones present in the primary sample are different from the ones in the relapse sample. However, this also comprises solutions in which the same subclone is present in both samples if the branches separating the two subclones are collapsed (Figure S3B). Similarly, these trees can also be collapsed into topologies of linear evolution (Figure S3B).

To select the most likely tree among the candidate topologies, we first require a good fit of the tumor stem. This is achieved by discarding trees in which more than 50% of the clonal (truncal) mutations are ambiguously mapped and, further, by discarding trees whose average squared error of clonal variant allele frequencies (VAFs) lay outside the 10% quantile of all candidate trees. We then assess the likelihoods of the remaining trees with a modified Bayesian Information Criterion (BIC) (Chen and Chen, 2008). Briefly, the modified BIC incorporates increasing model complexity with increasing numbers of parameters:

$$BIC_{\gamma} = -2 \log \mathscr{L}_n + v \log n + 2\gamma \log \mathscr{T}, \tag{Equation 10}$$

where n is the number of data points, v the number of parameters and τ a parameter accounting for increasing model complexity weighted by Υ. In our case the number of data points is the number of readcounts ($r_l^{ref} + r_l^{mut}$), the number of parameters is the number of subclones, K, and τ is obtained by summing up all possible values of s. We choose $\Upsilon = 0.9$ to stringently incorporate the increasing model complexity when increasing the number of parameters.

We fit all 96 trees consisting of up to three tumor subclones per sample (Figure S3A) and identified the most likely solutions based on the reliability of the estimated clonal mutations and the modified *BIC*, as explained above.

Parameter Estimation

Parameter estimations were performed on 500 mutated loci (including coding mutations and filled up by randomly chosen non-coding mutations). Subsequently, all mutations were mapped on the inferred tree structure. Upon fitting, copy number variations were manually inspected to identify large gains/losses and to adjust the solution in the case of inference problems due to high level amplifications or homozygous deletions.

We jointly estimated the parameters of matched primary and relapse samples with a maximum likelihood approach based on an expectation-maximization algorithm for different candidate trees. At a given evolutionary tree, a nested expectation step is followed by likelihood maximization from which the new input to the expectation step is generated. Both steps were iteratively repeated until convergence (required as $\sum (\mu^i - \mu^{i-1})^2 < 5 \times 10^{-4}$ where i is the index of the iteration). In order to identify the global maximum, optimization was repeated 100 times at random starting conditions for each candidate tree. Expectation and maximization steps are described in detail in the following.

Expectation

We initiated the algorithm with randomly chosen values for μ. In all following iterations, the parameter estimates obtained in the maximization step were given as input. In each expectation step, the expected counts of mutated and reference reads per subclone were iteratively calculated at each mutated locus after inferring the copy number state as follows:

Expectation Step: Copy Numbers

We assume that there is at most one dominating copy number change, $CN_{aberr,l}$, per locus and sample. This change does not have to be present in all subclones, allowing for tumor heterogeneity. While we allow different copy number changes to dominate the primary and the relapse sample at a specific locus, we do not allow for multiple copy number changes per locus within a sample.

We determined $CN_{aberr,l}$ from the normalized coverage ratios between tumor and blood along with the measured B-allele frequencies, BAF_l, in the tumor. To this end, we applied the following criteria:

- If no information on the coverage ratio was available, we assumed normal ploidy (2 on autosomes and female sex chromosomes, 1 on male sex chromosomes). If no information on the B-allele frequency was available, we assumed a B-allele frequency of 0.5 on autosomes and female sex chromosomes and of 0 on male sex chromosomes.

- We assumed that loci with coverage ratios in the interval [0.9, 1.1] and a *BAF* in the interval [0.45, 0.55] (or [0, 0.05] in case of male sex chromosomes) reflect normal copy number states, CN_{norm}, such that $CN_{aberr,l} = CN_{norm} = 2$ on autosomes and female sex chromosomes and $CN_{aberr,l} = CN_{norm} = 1$ on male sex chromosomes. The cutoffs were chosen based on the expected standard deviation of 8 % in Poisson distributed read counts at a coverage of 150x.
- At all other loci, we inferred the copy numbers and B-allele numbers by minimizing the squared errors between the expected and observed coverage ratios and B-allele frequencies. To this end, we started with a single copy number, which we iteratively increased. At each copy number we then tested different subclonal distributions $f \in F$ of the copy number change, where f is a vector $f = (f_1, f_2, \ldots, f_K)$, whose elements are binary indicators of a copy number change in the respective subclone, i.e. $f_i \in \{0,1\}$. The different combinations are restricted by the candidate tree and comprise solutions in which the same or two different copy number changes dominate the primary and the relapse sample, respectively. We computed the expected B-allele frequency for B-allele counts, $B_{aberr,l}$, in the interval $[0, CN_{aberr,l}]$

$$\mathrm{E}[\mathrm{BAF}_l] = \frac{\sum_i [f_i \mu_i B_{aberr,l} + (1 - f_i)\mu_i B_{norm}]}{\sum_i [f_i \mu_i CN_{aberr,l} + (1 - f_i)\mu_i CN_{norm}]}, \qquad \text{(Equation 11)}$$

and chose the B-allele count that minimized the squared error between expected and observed B-allele frequencies. Likewise, we computed the expected coverage ratio, $\mathrm{E}[cr_l]$, with

$$\mathrm{E}[\mathrm{cr}_l] = \frac{\sum_i [f_i \mu_i CN_{aberr,l} + (1 - f_i)\mu_i CN_{norm}]}{CN_{norm}}. \qquad \text{(Equation 12)}$$

We aborted the algorithm once $(\mathrm{E}[BAF_l] - BAF_{l,obs})^2 + (\mathrm{E}[cr_l] - cr_{l,obs})^2 < 0.01$ (the threshold of 0.01 corresponds to the expected Poisson noise at sequencing depths of 150x) and determined $B_{i,l}$ and $\pi_{i,l}$ for each $i \in \{1, 2, \ldots, K\}$ to

$$\begin{aligned} B_{i,l} &= B_{aberr,l} f_i + B_{norm}(1 - f_i) \\ \pi_{i,l} &= CN_{aberr,l} f_i + CN_{norm}(1 - f_i) \end{aligned} \qquad \text{(Equation 13)}$$

Note that while here only the most likely intratumoral distribution of a CNVs is selected, we accounted for alternative solutions for data representation and analysis as discussed below.

Expectation Step: SNVs and Small Indels

Having inferred the copy number state at locus l we determined the expected read counts for each possible combination of s_l and π_l (which are predefined by the candidate tree) with

$$\begin{aligned} \mathrm{E}\left[r_{i,l}^{ref}\right] &= p'^{ref}_{i,l} r_l^{ref}, \qquad p'^{ref}_{i,l} = \frac{p_{i,l}^{ref}}{\sum_{i'=1}^{K} p_{i',l}^{ref}}, \\ \mathrm{E}\left[r_{i,l}^{mut}\right] &= p'^{mut}_{i,l} r_l^{mut}, \qquad p'^{mut}_{i,l} = \frac{p_{i,l}^{mut}}{\sum_{i'=1}^{K} p_{i',l}^{mut}}, \end{aligned} \qquad \text{(Equation 14)}$$

where $p'^{ref}_{i,l}$ and $p'^{mut}_{i,l}$ are the conditional probabilities of a sampled reference or mutated read originating from SC_i provided that μ, s and π are known. We then computed the corresponding likelihood of μ, s and π as

$$\mathscr{L}_l\left(p_l \middle| r_l^{ref}, r_l^{mut}\right) = \sum_{\left(r_{i,l}^{ref}, r_{i,l}^{mut}\right)} \mathscr{L}_l\left(p_l \middle| r_{i,l}^{ref}, r_{i,l}^{mut}\right) \qquad \text{(Equation 15)}$$

and selected the solution with the highest likelihood (note that we considered alternative solutions for data representation and analysis also, if the best solution accounted for less than 90% of the total likelihood). Since DNA is fragmented before amplification and mapping, the read count distributions at different loci are independent of each other, so that the expectation step can be independently evaluated at each mutated locus. Of note, independence of measured coverage ratios is not guaranteed, since copy number variations can span multiple loci. This is already accounted for during segmentation and, thus, does not affect the inference procedure.

Maximization

We maximized the log-likelihood function (Equation 8) at the expected readcount distribution (Equation 14) w.r.t. μ. This was approached by summing up the log-likelihoods (Equation 8) at each locus and by introducing the constraint $\sum_{i=1}^{K} \mu_i = 1$ with a Lagrange multiplier before maximization:

$$\tilde{l} = \sum_l l_l + \lambda \left(1 - \sum_{i=1}^{K} \mu_i\right). \qquad \text{(Equation 16)}$$

After inserting Equation 5 into Equation 16, deviation with respect to μ_i and λ yields:

$$\frac{\partial \tilde{l}}{\partial \mu_i} = \sum_l \left(\frac{1}{\mu_i} \left(r_{i,l}^{ref} + r_{i,l}^{mut} \right) - \pi_{i,l} \frac{\sum_{i'=1}^{K} r_{i',l}^{ref} + r_{i',l}^{mut}}{\sum_{i'=1}^{K} \mu_{i'} \pi_{i',l}} \right) - \lambda, \quad \text{(Equation 17)}$$

$$\frac{\partial \tilde{l}}{\partial \lambda} = 1 - \sum_{i=1}^{K} \mu_i. \quad \text{(Equation 18)}$$

We find the maximum of the log-likelihood by setting Equations (17) and (18) equal to zero and solving for λ and μ:

$$\lambda \mu_i = \sum_l \left(r_{i,l}^{ref} + r_{i,l}^{mut} - \pi_{i,l} \mu_i \frac{\sum_{i'=1}^{K} r_{i',l}^{ref} + r_{i',l}^{mut}}{\sum_{i'=1}^{K} \mu_{i'} \pi_{i',l}} \right), \quad \text{(Equation 19)}$$

$$\sum_{i=1}^{K} \mu_i = 1. \quad \text{(Equation 20)}$$

Summing up Equation 19 over all subclones yields

$$\lambda \sum_{i=1}^{K} \mu_i = \sum_{i=1}^{K} \sum_l \left(r_{i,l}^{ref} + r_{i,l}^{mut} - \pi_{i,l} \mu_i \frac{\sum_{i'=1}^{K} r_{i',l}^{ref} + r_{i',l}^{mut}}{\sum_{i'=1}^{K} \mu_{i'} \pi_{i',l}} \right). \quad \text{(Equation 21)}$$

With Equation 20 this reduces to

$$\lambda = \sum_{i=1}^{K} \sum_l \left(r_{i,l}^{ref} + r_{i,l}^{mut} - \pi_{i,l} \mu_i \frac{\sum_{i'=1}^{K} r_{i',l}^{ref} + r_{i',l}^{mut}}{\sum_{i'=1}^{K} \mu_{i'} \pi_{i',l}} \right), \quad \text{(Equation 22)}$$

Rewriting Equation 19 yields

$$\mu_i = \frac{\sum_l r_{i,l}^{ref} + r_{i,l}^{mut}}{\sum_l \left(\pi_{i,l} \frac{\sum_{i'=1}^{K} r_{i',l}^{ref} + r_{i',l}^{mut}}{\sum_{i'=1}^{K} \mu_{i'} \pi_{i',l}} \right) + \lambda}, \quad \text{(Equation 23)}$$

which, after inserting Equation 22, reduces to

$$\mu_i = \frac{\sum_l \frac{r_{i,l}^{ref} + r_{i,l}^{mut}}{\pi_{i,l}}}{\sum_{i=1}^{K} \sum_l \frac{r_{i,l}^{ref} + r_{i,l}^{mut}}{\pi_{i,l}}}. \quad \text{(Equation 24)}$$

Ambiguous Solutions

To avoid bias in data interpretation due to potentially ambiguous solutions, we accounted for three types of ambiguity:

- CNVs. If model inference suggested two independent copy number changes in primary and relapse tumor, respectively, but the squared error of a joined solution was less than twice the least squared error, we accounted for the joined solution in data analysis and interpretation. Likewise, if the squared error for a clonal copy number change was less than twice the error of a subclonal copy number change, we accounted for the clonal solution.
- SNVs. If the location of a mutation to the phylogenetic tree was non-unique, i.e., if the best solution carried less than 90% of the total likelihood at this locus, we sorted solutions by decreasing likelihood and accounted for all solutions that jointly yielded at least 90% of the total likelihood in data analysis and interpretation.
- Tree structure. We accounted for all solutions with $BIC_{\Upsilon} \leq \min(BIC_{\Upsilon}) + 10$.

Simulated Data

To test the performance of phylogenetic tree reconstruction against a known "ground truth" computationally, we generated 100 test sets of up to three primary and recurrent subclones, respectively, according to the following algorithm:

- Sample between one and three primary and recurrent clones (K_{prim} and K_{rec})
- Sample the corresponding subclone sizes, μ_{prim} and μ_{rec}, at a minimal tumor cell content of 0.5
- Sample a random tree from Figure S3A
- Sample K_{prim} and K_{rec} nodes from this tree
- Sample between 1 and 200 mutations per subclone
- For each mutation sample a copy number change, π_l:
  - Normal copy numbers (two alleles) are weighted 15-fold
  - A unary copy number change (± 1) is weighted 2-fold
  - Copy number changes of up to +8 are weighted 1-fold each
- From the tree structure, sample the subclones that carry the copy number change, stored in the indicator vector π_l
- At each copy number change sample whether the mutation was affected by the copy number change; from this determine s_l
- Simulate the coverage ratios according to $cr_l = \frac{\sum_i \pi_i f_{i,l} \mu_i + 2(1 - f_{i,l})\mu_i}{2} + \mathcal{N}(\mu = 0.05, \sigma = 10^{-4})$ thus, adding Gaussian noise to the simulated coverage ratios
- Sample the read depth per locus from a Poisson distribution with $\lambda = 150$, corresponding to an average read depth of 150. Then, based on the read depth, sample the number of mutated reads from a binomial distribution with sampling probabilities according to Equation (5).

Modeling of Clonal Dynamics

To link genetic evolution and tumor growth, we considered a deterministic model of tumor growth and mutation accumulation. We assumed exponential tumor growth at rate λ-δ, where λ denotes the rate of cell division and δ the rate of cell death. The number of tumor cells, N, is modeled as

$$N(t) = e^{\lambda\left(1 - \frac{\delta}{\lambda}\right)t}, \qquad N(0) = 1 \qquad \text{(Equation 25)}$$

We implemented mutation accumulation at a constant rate μ per cell division, so that the number of mutations per cell, m, grows linearly with the number of divisions:

$$\dot{m} = \mu\lambda. \qquad \text{(Equation 26)}$$

Accordingly, the time it takes to accumulate m mutations in a tumor cell is

$$T(m) = \frac{m}{\mu\lambda}. \qquad \text{(Equation 27)}$$

Knowing μ, *m(t)* and the number of tumor cells, *N(t)*, we can estimate the ratio between cell death and division without information on the tumor age. Rewriting Equation 25 and inserting Equation 27 yields:

$$\tilde{\delta} = \frac{\delta}{\lambda} = 1 - \frac{\mu}{m(t)} \log N(t), \qquad \text{(Equation 28)}$$

where we defined $\tilde{\delta}$ as the death rate relative to cell divisions. To estimate $\tilde{\delta}$ from our data, μ, *m(t)* and *N(t)* were chosen as follows:

- We assumed a mutation rate between 0.26 x 10^{-8} to 1.06 x 10^{-8} mutations per cell division (Milholland et al., 2017). The upper boundary corresponds to a four-fold increase in somatic mutation rate, accounting for a drop in the proportion of the mutational signature 1 (linked to cell divisions) between tumor stem and tips (Figure S5J).
- We conservatively estimated the number of mutations per tumor cell at diagnosis as the average number of non-clonal mutations in all subclones of the primary tumor. Note that the mutations present in a subclone are shared by all cells of the subclone and thus have been accumulated in a single cell.
- Finally, we estimated a tumor size of approximately 10^9 - 10^{10} cells at diagnosis. This estimate has previously been suggested as the number of tumor cells per cubic centimeter (Del Monte, 2009; DeVita et al., 1975) and is in agreement with a brain tumor size of 20 - 80 cm^3 and 10^{12} glia cells per brain (Goldberg-Zimring et al., 2005; Herculaono-Houzel et al., 2006; Milo et al., 2010; Pakkenberg et al., 1997) (corresponding to a brain size of approximately 1500 cm^3, see Drachman, 2005).

Selective Advantage of *TERT* Promoter Mutations

To estimate the selective advantage provided by canonical *TERT* promoter mutations, we modeled its random acquisition and subsequent clonal expansion. The model samples the time of occurrence of the *TERT* promoter mutation from a Poisson process with given mutation rate. From this point onward, the *TERT* promoter-mutant subclone grows faster than *TERT* promoter-wildtype tumor cells. The model simulation is terminated when the tumor reaches the characteristic size of surgical resection. At this end point, the *TERT* promoter-mutant subclone may have reached clonality or may still be subclonal (although it would eventually become

clonal if the tumor were allowed to grow for another year or so). Repeating this simulation will therefore result in a distribution for the *TERT* promoter-mutant tumor fraction that will be compared with the experimental data. The free parameter in this model is the selective advantage conferred by the *TERT* promoter mutation. This parameter will be adjusted such that the model matches the data, thus providing an estimate of the selective advantage conferred by the *TERT* promoter mutation.

We began by assessing the probability of capturing the mutation after a certain number of cell divisions. The probability of at least one mutation (denoted as *TERT**) after n_{div} divisions is given by

$$P(TERT*) = 1 - \left(1 - 2\mu_{\mathrm{bp}}\right)^{n_{\mathrm{div}}}, \qquad \text{(Equation 29)}$$

where μ_{bp} denotes the per base substitution rate per cell division. The mutation probability is scaled by a factor of 2 accounting for the two canonical *TERT* promoter mutations recurrently observed in glioblastoma (chr5, 1,295,228C > T and 1,295,250C > T). The number of divisions, n_{div} is a time dependent function, modeled by

$$\dot{n}_{\mathrm{div}} = \lambda N, \qquad \text{(Equation 30)}$$

which, using Equation 25 can be solved by

$$n_{\mathrm{div}} = \frac{1}{1-\tilde{\delta}}\left(e^{(1-\tilde{\delta})t} - 1\right). \qquad \text{(Equation 31)}$$

Inserting this into Equation 29 we obtain the probability distribution of at least one *TERT* promoter mutation at timepoint *t*. We modeled the effect of *TERT* promoter mutations by a decrease in cell death since these mutations have been linked to increased cellular survival (Chiba et al., 2017). Consequently, the expansion of the *TERT* mutated tumor fraction, N_{TERT}, is modeled by

$$N_{\mathrm{TERT}}(t) = \begin{cases} 0 & t < T_{0,\mathrm{TERT}} \\ e^{\left(1-\tilde{\delta}_{\mathrm{TERT}}\right)\left(t - T_{0,\mathrm{TERT}}\right)} & t \geq T_{0,\mathrm{TERT}} \end{cases} \qquad \text{(Equation 32)}$$

The expansion of the tumor founder population is modeled by Equation 25. The total tumor size consequently equals the sum of Equations 25 and 32. Since *TERT* promoter mutations were found clonally in ≥ 2/3 of the tumors, the estimated tumor cell death fraction, $\tilde{\delta}$ (Equation 28) must hold true for *TERT* mutated cells. Accordingly, we fixed the lower boundary $\tilde{\delta}_{\mathrm{TERT,\,min}}$ based on Equation 28 and for each $\tilde{\delta}_{\mathrm{TERT,\,min}} \leq \tilde{\delta}_{\mathrm{TERT}} \leq 0.999$ evaluated the death rate of the founder population, $\tilde{\delta}_0$. To do this we scanned the range $\tilde{\delta}_{\mathrm{TERT}} \leq \tilde{\delta}_0 \leq 0.999$ and at each value sampled 1,000 instances of the timepoint of the *TERT* promoter mutation, $T_{0,TERT}$, from Equation 29 (assuming single base substitution rates of 0.26 x 10^{-8} to 1.06 x 10^{-8} (Milholland et al., 2017) and a tumor size of 10^9 cells, as before). We then evaluated the goodness of fit at each parameter combination by $\mathscr{X}^2$ minimization, comparing the mean and variance of the simulated and measured *TERT* mutated tumor fraction (the uncertainties of the mean and the variance in the measurement were estimated using bootstrapping with 10,000 resampling steps). Parameter combinations with $\Delta\mathscr{X}^2 \leq 5.99$, corresponding to the 95% confidence interval of the Chi^2-distribution yield equally good fits and we selected the values of $\tilde{\delta}_0$ and $\tilde{\delta}_{\mathrm{TERT}}$ from $\min_{\tilde{\delta}_0,\tilde{\delta}_{\mathrm{TERT}}} \big| \Delta\mathscr{X}^2 \leq 5.99$.

Finally, we assessed the selective advantage before and after the *TERT* promoter mutation, s_0 and s_{TERT}, as (Bozic et al., 2016)

$$s_0 = 1 - 2\frac{\tilde{\delta}_0}{1+\tilde{\delta}_0} \qquad \text{(Equation 33)}$$

$$s_{\mathrm{TERT}} = 1 - \frac{\tilde{\delta}_{\mathrm{TERT}}}{1+\tilde{\delta}_{\mathrm{TERT}}}\,\frac{1+\tilde{\delta}_0}{\tilde{\delta}_0}. \qquad \text{(Equation 34)}$$

QUANTIFICATION AND STATISTICAL ANALYSIS

Statistical Tests

To measure differences in the mutational burden of primary and relapsed glioblastomas, we employed a two-sided Welch two sample t-test on the 17 non-hypermutated tumor pairs. The distribution of methylated and unmethylated *MGMT* promoters between tumors with mono- or oligoclonal relapse origins was assessed with a hypergeometric distribution (n=21, corresponding to the tumors of the discovery set). Differential gene expression between tumors and normal brain tissue was analyzed with the R package DESeq2 1.18.1 (Love et al., 2014); differential expression was accepted for Benjamini-Hochberg-corrected p values < 0.01.

All statistical parameters shown in figures are detailed in the figure legends.

Software

Phylogenetic inference and modeling of evolutionary dynamics were performed on R 3.3.1 (R Core Team, 2017), using the libraries doParallel, foreach and phangorn. The R libraries AnnotationsDbi, DESeq2, FlowSorted.DLPFC.450k, FlowSorted.Blood.450k, GenomicRanges, Hmisc, Homo.sapiens, MCP-counter, minfi, phangorn, phyloTop, phytools, YAPSA and xlsx were used for data analysis and the libraries beeswarm, colorlovers, colorspace, ComplexHeatmaps, ggplot2, igraph, pheatmap, plotrix and

RColorBrewer were used for plotting. Plots were redesigned in Adobe Illustrator CS5. All other software used is mentioned in Method Details.

DATA AND SOFTWARE AVAILABILITY

The accession number for the sequencing data reported in this paper is European Genome-phenome Archive (EGA): EGAS00001003184. R codes for phylogenetic inference and modeling of clonal dynamics are available as supplementary files to this paper (Data S1) and from https://github.com/hoefer-lab/phy_clo_dy. In-house pipeline for detection of structural variants (SOPHIA) is available from https://bitbucket.org/utoprak/sophia.